



UNIVERSITY OF LEEDS

# Numerical Simulations of Dusty Colliding Wind Binaries



Joseph Eatson

University of Leeds

School of Physics and Astronomy

Submitted in accordance with the requirements for the degree of

*Doctor of Philosophy*

September, 2021

This thesis is dedicated to my Mum, without her help these past 26 years, there's no way I would have written this.

I'll pay you back I promise!

## Acknowledgements

**If you're reading this ahead of time and wondering where you are, don't worry, I'm getting to you, just writing the thesis first!**

No good thesis<sup>1</sup> wouldn't be complete without a commitment to the authors friends. I first met some of you on literal day one of my undergraduate degree in Leeds, it's really quite incredible how you've all tolerated my nonsense for so long. From essentially forcing my way into Rob's house so I could cook some disastrous fried chicken, to playing Super Smash Bros. all night long on it's release day, to watching trashy movies over the internet at the height of the pandemic, these are moments I'll treasure for the rest of my life. Thank you all, for making me so happy these last 9 years. In particular, those who are still in Leeds, Rob, Matt, Kelsie and Alex; as well as those who aren't, Martin, Caz, Andy, and Devon.

To my partner Pruthvi, I cannot stress how unlikely it is that the two of us even met; two people finding each other on esoteric circles of the internet is like two particles colliding in the tenuous interstellar medium, if you'll excuse the extremely trashy metaphor. You've been supportive, helpful, and the most wonderful partner anyone could ask for; I truly am blessed to know you and love you.

I would also like to thank the wonderful team at Leeds' ARC High Performance Computing department, considering the bulk of this work involves many 3D numerical simulations my use of ARC 4's compute nodes can be described as somewhere from "excessive" to "taking the piss". I also apologise for running my earlier simulations on the login nodes for multiple days, I swear it was an accident.

Finally, I would like to thank Leandro Panizzon and his wife, Margarita, though Methylphenidate was originally synthesised by him to treat her low blood pressure, it also works quite well for dragging my attention-deficit riddled brain through this PhD.

---

<sup>1</sup>Though the quality of this one is debatable.

## Abstract

---

# CONTENTS

<b>1</b>	<b>Introduction and Motivation</b>	<b>1</b>
<b>2</b>	<b>Background</b>	<b>3</b>
2.1	Early-Type Stars . . . . .	4
2.1.1	OB-type stars . . . . .	4
2.1.2	Wolf-Rayet stars . . . . .	7
2.2	Stellar Winds . . . . .	8
2.2.1	Stellar winds in low mass stars . . . . .	9
2.2.2	Stellar winds in high mass stars . . . . .	9
2.2.3	The CAK formalism . . . . .	12
2.3	Interstellar Dust . . . . .	12
2.3.1	The importance of interstellar dust . . . . .	12
2.3.2	Interstellar dust in massive star systems . . . . .	12
2.4	Colliding Wind Binary Systems . . . . .	12
2.4.1	The Wind Collision Region . . . . .	13
2.4.2	Cooling in the WCR . . . . .	14
2.4.3	Dust formation in CWB systems . . . . .	18
2.4.4	Important WCd systems . . . . .	18
2.4.5	Contemporary research in extragalactic low-metallicity WCd systems . . . . .	18
<b>3</b>	<b>Methodology &amp; Numerical Simulation</b>	<b>19</b>
3.1	The Purpose of Numerical Simulations . . . . .	20
3.2	The Mathematics of Numerical Simulations . . . . .	20
3.3	Computational Hydrodynamics . . . . .	20
3.4	The Athena++ Hydrodynamical code . . . . .	20

## CONTENTS

---

3.5	Simulating CWB systems . . . . .	20
3.5.1	Assumptions . . . . .	20
3.6	Cooling in numerical simulations . . . . .	20
3.6.1	Plasma cooling . . . . .	20
3.6.2	Dust cooling . . . . .	20
3.6.3	Exact cooling method . . . . .	25
3.7	The BODMAS Advected Scalar Dust Model . . . . .	25
3.8	Contemporary Dust Models . . . . .	25
3.8.1	The Hendrix dust model . . . . .	25
3.9	Future dust models . . . . .	26
<b>4</b>	<b>A Parameter Space Exploration of Dust Formation</b>	<b>27</b>
4.1	Introduction . . . . .	28
4.2	Simulating CWB Systems . . . . .	30
4.2.1	Mesh refinement . . . . .	31
4.2.2	Wind mapping and orbits . . . . .	31
4.2.3	Gas and dust cooling . . . . .	32
4.2.4	Numerical modelling of dust through advected scalars . . . . .	35
4.3	Model Parameters . . . . .	38
4.3.1	Cooling . . . . .	39
4.3.2	Wind momentum ratio . . . . .	39
4.3.3	Separation distance . . . . .	39
4.4	Momentum ratio variation . . . . .	41
4.5	Separation variation . . . . .	41
4.5.1	Adiabatic flow . . . . .	41
4.5.2	Dust production yields . . . . .	41
4.5.3	Periodicity within a circular orbit . . . . .	41
4.5.4	Wind mixing within the WCR . . . . .	41
<b>5</b>	<b>Hydrodynamical Simulations of WCd Systems</b>	<b>43</b>
5.1	Introduction . . . . .	44
5.2	Methodology . . . . .	45
5.2.1	Hydrodynamics . . . . .	45
5.2.2	Dust model and cooling . . . . .	45

## CONTENTS

---

5.2.3	Simulated systems . . . . .	46
5.2.4	Radiative transfer modelling . . . . .	49
<b>6</b>	<b>Final Notes and Conclusion</b>	<b>51</b>
<b>A</b>	<b>Astrophysical Shocks</b>	<b>53</b>
	<b>References</b>	<b>54</b>



## CONTENTS

---

# LIST OF FIGURES

2.1	Planck's law radiance comparison with resonance lines . . . . .	10
2.2	M1-67 nebula around WR 124 . . . . .	11
2.3	$\rho_w$ comparison of main sequence winds . . . . .	13
2.4	WC & solar abundance plasma cooling curves . . . . .	15
2.5	Dust cooling vs. plasma cooling . . . . .	16
2.6	$H_{el}$ and $H_{coll}$ comparison . . . . .	17
3.1	Dust lookup table methods comparison . . . . .	22
3.2	Electron transparency method accuracy - $h_e$ . . . . .	23
3.3	Electron transparency method accuracy - $H_{el}/H_{coll}$ . . . . .	24
3.4	Electron transparency method accuracy - $\Lambda_d$ . . . . .	24
3.5	Ionisation fraction for OB and WC stars . . . . .	26
4.1	WR and OB $\Lambda(T)$ cooling curves . . . . .	34
4.2	Comparison of $h_e$ integration and approximation for increasing gas temperature .	35
4.3	Comparison of dust cooling parameter $\Lambda(T)$ . . . . .	36
4.4	OB and WR electron-ion ratios . . . . .	37
5.1	Orbital path comparison . . . . .	48
5.2	$\chi$ change over system orbit . . . . .	49

## LIST OF FIGURES

---

# LIST OF TABLES

2.1	Stellar wind comparison . . . . .	12
2.2	Cooling processes at various temperature ranges . . . . .	14
3.1	Dust cooling calculation comparison . . . . .	25
4.1	Abundances used for OB and WC stars . . . . .	33
4.2	Wind properties of the baseline system . . . . .	38
4.3	Baseline system orbital properties . . . . .	39
4.4	Momentum ratio modification parameters . . . . .	40
4.5	Parameters of simulations varying separation distance. . . . .	41
5.1	Wind properties of systems simulated in this paper. . . . .	47
5.2	Orbital properties of systems simulated in this paper. . . . .	47

## Abbreviations

List of common abbreviations, if an abbreviation is important enough to warrant a section in this thesis, the section will be referenced.

BODMAS	Binary Orbit Dust Model with Accretion and Sputtering	Section <a href="#">3.7</a>
CWB	Colliding Wind Binary	Section <a href="#">2.1.1</a>
GMC	Giant Molecular Cloud	Section <a href="#">2.1.1</a>
LBV	Luminous Blue Variable	Section <a href="#">2.1.1</a>
OB	O or B type star	Section <a href="#">2.1.1</a>
RSG	Red Supergiant	Section <a href="#">2.1.1</a>
WC	WR Carbon Phase	Section <a href="#">2.1.2</a>
WCd	Dust forming WC star	Section <a href="#">2.4.3</a>
WCR	Wind Collision Region	Section <a href="#">2.4.1</a>
WN	WR Nitrogen Phase	Section <a href="#">2.1.2</a>
WO	WR Oxygen Phase	Section <a href="#">2.1.2</a>
WR	Wolf-Rayet	Section <a href="#">2.1.2</a>

## Common Symbols

List of common symbols, if symbol requires a derivation, the appropriate equation within this thesis will be referenced. If the symbol is a unit, the value in CGS units will be provided instead.

$a$	Grain radius	
$C$	Courant-Friedrichs-Lewy condition	
$h_e$	Electron transparency	Section <a href="#">2.4.2</a>
$H_{coll}$	Grain heating rate due to ions	
$H_{el}$	Grain heating rate due to electrons	
$L_*$	Stellar luminosity	
$M_*$	Stellar mass	
$\dot{M}$	Mass loss rate	
$v_\infty$	Wind terminal velocity	
$z$	Dust-to-gas mass ratio	
$\eta$	Wind momentum ratio	
$\Lambda(T)$	Plasma Cooling function	
$\Lambda_d(h, a, T)$	Dust cooling function	
$\xi$	Grain sticking efficiency	
$\theta_c$	WCR conic opening angle	Equation <a href="#">2.10</a>
$\tau_{KH}$	Kelvin-Helmholtz timescale	Equation <a href="#">2.1a</a>
$\tau_{ff}$	Free-fall timescale	Equation <a href="#">2.1b</a>
$\tau_{cool}$	Cooling timescale	Equation <a href="#">2.11a</a>
$\tau_{esc}$	Escape timescale	Equation <a href="#">2.11b</a>
$\chi$	Cooling parameter	Equation <a href="#">2.12</a>
$M_\odot$	Solar mass	$1.988 \times 10^{33} \text{ g}$
$M_\odot \text{ yr}^{-1}$	Solar mass per year	$6.301 \times 10^{25} \text{ g s}^{-1}$
$L_\odot$	Solar Luminosity	$3.828 \times 10^{33} \text{ erg s}^{-1}$

AU	Astronomical Unit	$1.496 \times 10^{13}$ cm
pc	Parsec	$3.086 \times 10^{18}$ cm
“warm”	Warm temperature regime	Between $10^4$ and $10^5$ K, personally

---

# CHAPTER 1

---

Introduction and Motivation



## 1. INTRODUCTION AND MOTIVATION

---

---

# CHAPTER 2

---

Background

## 2. BACKGROUND

---

### 2.1 Early-Type Stars

The term Early-type stars is quite possibly the epitome of bad naming conventions in astrophysics, it's a very old term, coming from the dawn of astrophysics itself, quite opaque as to what it means, and also by definition *completely wrong*. In fact it is one of the most wrong pieces of terminology I can think of.<sup>1</sup> The first generation of astrophysicists found themselves asking very important questions such as “what even *are* stars” and “what possible mechanism can allow a star to burn for so long?” Each of these questions was rather pressing for the burgeoning field, and the scientific community was aching for an answer.

Of course, like all pressing questions of the 19<sup>th</sup> century, it fell to Lord Kelvin to provide a convincing but incorrect answer. Kelvin assumed that gravitational collapse was the mechanism for a stars long-term heating, with younger, “early” type stars shining the brightest. Not only was the mechanism incorrect, but typically older main sequence stars are more luminous than their younger counterparts of a similar mass! However, as is the case with astrophysical terminology, the term stuck, to the confusion of many young astrophysicists.

Instead, we now know that stars produce their energy through fusion. These reactions vary from sub-stellar deuterium and lithium burning, to main sequence p-p & CNO hydrogen burning processes, and finally to the triple- $\alpha$  and other exotic fusion processes for evolved massive stars. The more massive the star the greater the internal pressure, allowing for more exotic fusion processes. The bigger a star, the greater the core pressure and temperature, as all fusion reactions are highly dependent on temperature, stars with only a few dozen solar masses are thousands of times more luminous than our sun, but only live a fraction of the time (Carroll & Ostlie, 2014).

#### 2.1.1 OB-type stars

And with that we shift our gaze to high-mass stars, with the most massive of all being the O and B type stars, these are extremely luminous ( $\sim 10^4 L_{\odot}$ ), and relatively short lived ( $\sim 10$  Myr) stars. The age-old adage of a candle burning twice as bright lasting half as long applies to our studies of the cosmos, but it is more apt to compare a candle and a stick of dynamite when considering stars on opposing ends of the Harvard classification system.

The most common formation mechanism of stars is through the collapse of a giant molecular

---

<sup>1</sup>Aside from astrophysicists calling something “warm”, of course. That can quite literally mean anything from 10 to 10,000 Kelvin, depending on who you ask, what they're writing about, or how they're feeling at that particular moment. In fact, I'll probably end up falling into this same trap somewhere in this thesis as well!

cloud<sup>1</sup>, an enormous cool cloud many parsecs across with a mass of around  $10^4 M_\odot$ . As this GMC collapses and radiates energy, lowering the radius of thermostatic equilibrium for the cloud, as collapsing progresses the cloud fragments into many smaller regions with a critical density, capable of collapsing further, forming a star. The collapse of a GMC can be described with a series of timescale. First, the Kelvin-Helmholtz timescale,  $\tau_{KH}$ , which describes the timescale required for the radiating cloud to collapse. The second important timescale is the free-fall timescale,  $\tau_{ff}$ , which is the time taken for a cloud to collapse. These timescales are described by the following equations:

$$\tau_{KH} \approx \frac{GM_*^2}{R_* L_*}, \quad (2.1a)$$

$$\tau_{ff} = \sqrt{\frac{3\pi}{32G\rho}}, \quad (2.1b)$$

where  $M_*$  is the protostellar mass,  $R_*$  is the protostellar radius,  $L_*$  is the protostellar luminosity, and  $\rho$  is the mean density of the collapsing cloud (Ward-Thompson & Whitworth, 2011).

Perhaps the most important distinction between massive star formation and its better understood counterpart is as a young protostar approaches the main sequence, the KH timescale is less than the free-fall timescale, meaning the material at the center of the collapsing cloud begins fusion while the bulk of core has collapsed onto the site of the future star. This burgeoning star begins to drive the weakly gravitationally coupled collapsing material away due to its sheer luminosity, driving this material outwards, causing it to accrete and shock material within the GMC.

Another important consideration is the role of angular momentum as the star collapses. The particularly massive cloud involved in massive star formation is more prone to fragmentation, meaning that massive stars typically form with an orbital partner, whilst approximately 2/3<sup>rds</sup> of low-mass stars are part of a binary or multiple system, this value is near-total. As such, the environment within an OB association after star formation consists of numerous young stars in tightly-knit groups disrupting the entire local area.<sup>2</sup>

Above a stellar mass of  $1.3M_\odot$  pressures and temperatures within a stellar core favour the fusion of hydrogen into helium through the catalytic CNO cycle, instead of the more direct p-p

---

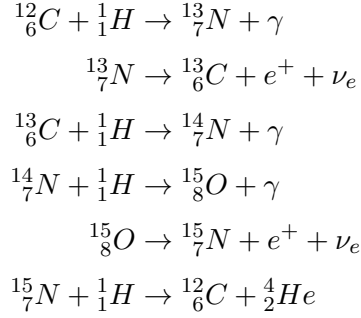
<sup>1</sup>GMC

<sup>2</sup>This is a bit like living in Headingley, Hyde Park, or any other area with lots of Undergraduates.

## 2. BACKGROUND

---

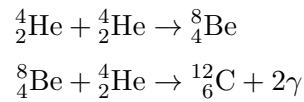
fusion process.



The reaction rate of CNO rises much faster, resulting in a convective core, surrounded by a radiative envelope (Salaris & Cassisi, 2005). This is the driving force behind the incredible luminosities of an OB star as it hurtles along the main sequence.

Unfortunately for massive stars, pesky fundamental laws such as the conservation of energy come into play. With only an order of magnitude or two of additional mass more than our sun and shining  $10^4$  times as brightly, this curtails the life of the brightest stars to lifespans not much more than  $10^7$  years. If we define a galactic year as the time it takes for a star to orbit the Milky Way, these poor stars don't even make it to their first birthdays, which is quite sad really.<sup>1</sup>

As the available hydrogen begins to become depleted, the lowering reaction rates force the star to shrink, this raises the internal temperature until the core begins to burn helium through the triple- $\alpha$  process:



The sudden spike in energy radiating from the core shifts the calculus of hydrostatic equilibrium in the favour of outward forces, causing the star to rapidly expand in the form of a Red Supergiant or Luminous Blue Variable (Ryan & Norton, 2010). During this phase the energy output of the star is even greater, with a timescale of  $\sim 10^6$  years, this is only temporarily prolonging the life of the star, which will inevitably begin burning heavier and heavier elements,

---

<sup>1</sup>Continuing this analogy our sun can drink, might have voted if they felt like it, and may be racking up vast quantities of student debt.

faster and faster. Once the star starts producing iron its fate is sealed, the star stops fusing, and collapses, annihilating itself in the form of a supernova and leaving behind a remnant of its core in the form of a neutron star or black hole (Ward-Thompson & Whitworth, 2011).

Whilst the stars end is as inevitable as it is violent, the intermediate stage as the star leaves the main sequence is in itself extremely interesting, and for the context of this thesis, no product of this stage is more interesting than the Wolf-Rayet.

### 2.1.2 Wolf-Rayet stars

As we now know, Wolf-Rayets<sup>1</sup> are evolved forms of O-type stars, and are a short lived component of the life-cycle of massive stars, typically lasting for around  $5 \times 10^5$  years (Crowther, 2007). Despite this relatively transient length of this stage, the influence of a WR star on its local medium is extremely outsized. WR stars in particular are known for having dense, fast winds, typically between 2 and 3 orders of magnitude than their main sequence O-type progenitors, with mass loss rates on the order of  $10^{-5} M_{\odot} \text{ yr}^{-1}$  and wind velocities of  $1.5 \times 10^3 \text{ km s}^{-1}$ . This extremely dense wind is driven by the highly energetic helium burning core, which is luminous enough as to drive away the outer layers of the stars envelope, exposing the core. The observed spectroscopic lines are due to heating of the envelope from the core, which is enriched with by-products of hydrogen and helium burning, the lack of hydrogen lines is due to the stars evolved nature, as all the hydrogen has been burned, there is simply nothing left to observe!

Wolf-Rayet stars can be subcategorised through spectroscopic observation, which indicates enrichment in a particular element, the 3 major sub-types, WN, WC and WO are defined by their strong nitrogen, carbon and oxygen lines respectively. The important distinction between WN and WC/WO stars is that WN stars are enriched through hydrogen burning, whilst WC and WO are enriched through the by-products of helium burning (Vink, 2015).

As a Wolf-Rayet continues to lose its envelope, additional products of fusion processes are dredged up from the centre of the star. In the case of the WN sub-type, the broad nitrogen lines correspond to the outer layer of the envelope, enriched through the CNO process; after this outer envelope is cast off, the remainder of the envelope exhibits carbon and oxygen lines, indicating enrichment from the triple- $\alpha$  process. Finally, the star evolves further and the innermost region of the envelope is revealed, observed as the strong oxygen lines of a WO sub-type (Neugent & Massey, 2019; Oswalt & Barstow, 2013).

As an O-type star transitions to a Wolf-Rayet, it typically undergoes an intermediary LBV

---

<sup>1</sup>Abbreviated to WR.

## 2. BACKGROUND

---

or RSG stage as helium burning begins, this is mass dependent, with the various transitional states described by Crowther, 2007:

$$\begin{aligned} \text{O} &\rightarrow \text{LBV/RSG} \rightarrow \text{WN(H-poor)} \rightarrow \text{WC} \rightarrow \text{SN 1b}, & \text{for } 25 \text{ M}_{\odot} < M_{\text{WR}} < 40 \text{ M}_{\odot} \\ \text{O} &\rightarrow \text{LBV} \rightarrow \text{WN(H-poor)} \rightarrow \text{WC} \rightarrow \text{SN 1c}, & \text{for } 40 \text{ M}_{\odot} < M_{\text{WR}} < 75 \text{ M}_{\odot} \\ \text{O} &\rightarrow \text{WN(H-rich)} \rightarrow \text{LBV} \rightarrow \text{WN(H-poor)} \rightarrow \text{WC} \rightarrow \text{SN 1c}, & \text{for } M_{\text{WR}} > 75 \text{ M}_{\odot} \end{aligned}$$

Wolf-Rayet stars are important in the context of this work due to their outsized influence within a WR+OB binary pair. The WR component of a WR+OB binary has an outsized contribution in returning material to the ISM, whilst also dominating the dynamics of the system, with their winds completely overpowering those of their O-type neighbours. In some cases, the dense, fast wind from the WR can collide with the much more tenuous wind from its partner, forming a strong shock, and a variety of fascinating effects. However, I wouldn't want to spoil too much too soon, but you can skip ahead to section 2.4, where this phenomena is covered in more detail.

### 2.2 Stellar Winds

Stellar winds have already been discussed to some extent in the previous section, however, due to the significance of winds within this body of work, further detailing of winds must be discussed to gain a better understanding of the dynamics of Colliding Wind Binary systems. This section will cover in brief the study of stellar winds, particularly driving mechanisms from low and high mass stars.

The study of stellar winds is of course, rather hard from our vantage point on Earth, as direct observation of a non-stellar solar wind is difficult, and sampling of the winds themselves significantly more difficult than that due to the inconvenient distances involved in interstellar travel. Because of this, extrasolar wind properties are derived from spectrography, with velocities derived through Doppler shift. The important parameters to consider in a wind, especially for this thesis, is the mass loss rate,  $\dot{M}$ , the wind terminal velocity,  $v^{\infty}$  and the abundances within the wind.

$$\frac{dM}{dt} = 4\pi\rho(\mathbf{r})v(\mathbf{r})r^2, \tag{2.5}$$

$$\rho_w = \frac{\dot{M}}{4\pi v_\infty r^2}, \quad (2.6)$$

This section will cover the different driving mechanisms winds from low and high mass stars, the typical wind parameters and driving mechanisms are broken down in table 2.1.

### 2.2.1 Stellar winds in low mass stars

Low mass stellar main sequence stellar winds are quite paltry for an astrophysical phenomenon, the sun, for instance, drives thin, comparatively slow winds, with a mass loss rate of  $\sim 10^{-14} \text{ M}_\odot \text{ yr}^{-1}$  and a terminal velocity of  $400 \text{ km s}^{-1}$ . The mechanism behind this is gas pressure from coronal heating, with outward pressure driving gas within stellar atmosphere away from the star, this results in a transonic wind that quickly reaches its terminal velocity as the coronal temperature and subsequent pressure quickly drops off.

As a low mass star exits the main sequence, ballooning in size to become a red giant, the density of the stellar wind increases dramatically.

As dust condenses in the upper atmosphere of the red giant, these grains can readily adsorb photons, utilising radiation pressure to be driven away from the more luminous giant star, easily achieving escape velocity against the low surface gravity of the red giant. Gas is also driven away, coupled to the dust, this provides an efficient form of momentum transfer, allowing for an extremely dense albeit slow stellar wind

### 2.2.2 Stellar winds in high mass stars

In the same way that high-mass stars are many orders of magnitude brighter than their low mass counterparts despite a comparatively low increase in mass, the same can be said of the density of stellar wind. A main sequence OB star typically has a mass loss rate of  $10^8 \text{ M}_\odot \text{ yr}^{-1}$ , 6 orders of magnitude higher than a solar mass star. This discrepancy in wind density cannot be explained by stronger coronal heating, in fact, the lack of a convective envelope ensures that coronal heating is not even feasible as a driving method! Instead we must look towards the higher luminosities that massive stars exhibit to find a suitable mechanism.

Simple radiation pressure from these stars would not be enough to explain the observed dense, highly supersonic winds emanating from these massive stars.

Resonance lines were also considered, a photon with an energy equal to the excitation energy of an ion is absorbed by that ion, gaining the momentum of this ion. The ion subsequently de-excites over a timescale on the order of  $10^{-8} \text{ s}$ , emitting a photon at a random angle relative



## 2. BACKGROUND

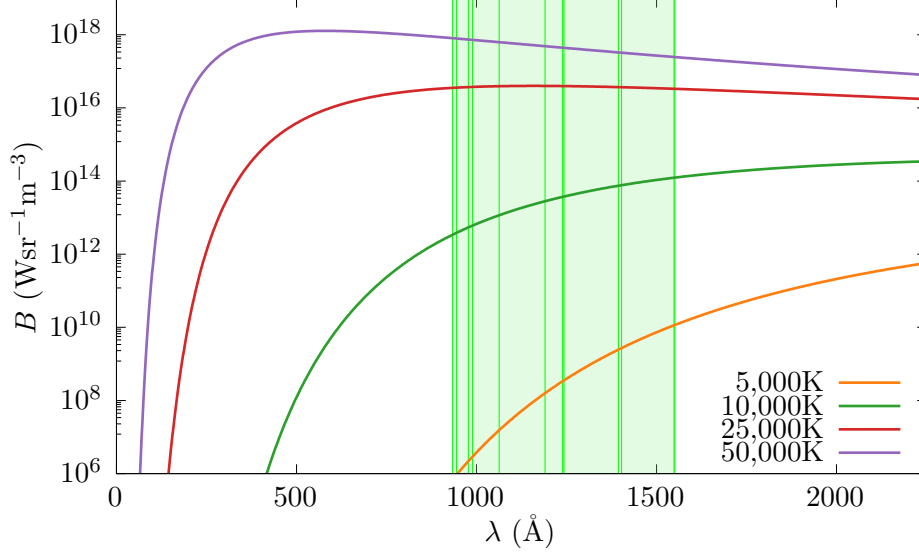


**Figure 2.1:** Spectral radiance against wavelength for black body objects at various effective temperatures,  $T_{\text{eff}}$ , a series of wavelengths corresponding with important resonance lines in table 1 of Lucy and Solomon, 1970 have been included. As temperature increases the spectral radiance at resonance line wavelengths dramatically increases, with a minimum of 6 orders of magnitude difference between the effective temperatures of a solar equivalent main sequence star and an O-type main sequence or Wolf-Rayet star.

to the radial direction,  $\alpha$ . The resultant change in radial velocity,  $\Delta v_r$ , for the adsorption of a photon at the resonance frequency  $\nu_0$  is

$$\Delta v_r = v_r'' - v_r = \frac{h\nu_0}{mc}(1 - \cos \alpha), \quad (2.7)$$

where  $v_r''$  is the radial velocity after the absorption and emission events, and  $m$  is the ion mass. These ions are accelerated away from the star, along with the rest of the stellar wind which is coupled through Coulomb forces. The opacity of such resonance lines can be up to six orders of magnitude larger than the opacity of a Thomson scattering event (Lamers & Cassinelli, 1999). Additionally, this effect is not observed in low-mass stars, whose spectra typically peak in the visible light, while resonance lines typically have energies equivalent to UV photons (figure 2.1). O-type stars and Wolf-Rayets, however, emit much of their radiation within the UV range.

Early computations involving resonance lines from Lucy and Solomon, 1970 provided a more reasonable mass loss rate calculation, but were still off by approximately two orders of magnitude.

Building off of the work by Lucy, a vital paper in the solidification of radiative lines as the main driving mechanism behind massive star outflows was produced by Castor, Abbott and Klein<sup>1</sup>. This work more accurately computed the influence due to resonance lines,

(Castor et al., 1975).

As previously mentioned, evolved massive stars progress into a helium burning WR phase, at this point, mass loss rates due to radiative line driving are extreme, in the order of  $10^{-5} M_{\odot} \text{ yr}^{-1}$ . This outsized influence on the local medium can be seen in the production of ejecta nebula, such as M1-67 produced by WR 124, as seen in figure 2.2.

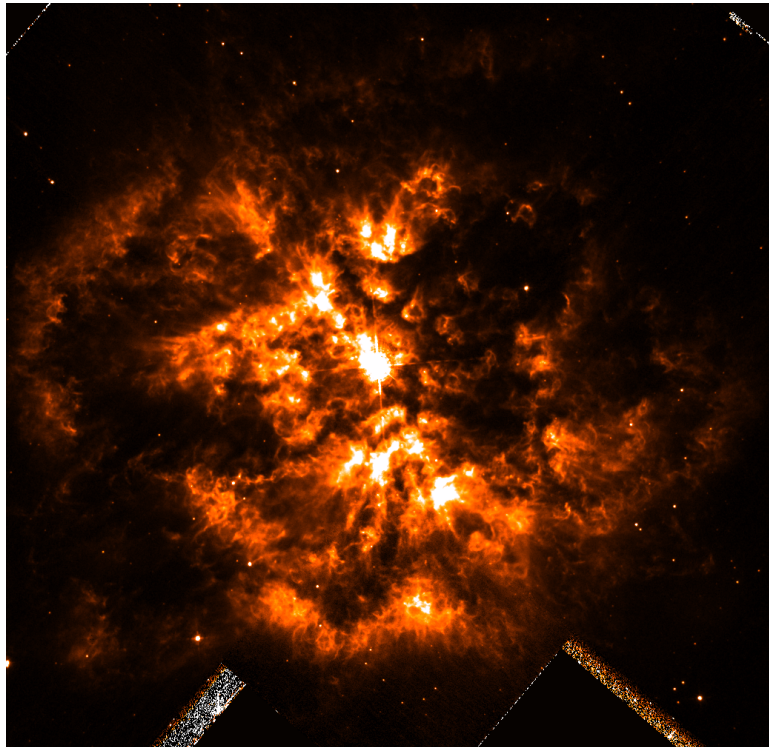


**Figure 2.2:** Reduced Hubble WFPC2 instrument data of the WN star WR 124, its extreme mass loss is currently producing an ejecta nebula, M1-67 (Marchenko et al., 2010).

---

<sup>1</sup>Hereafter abbreviated as CAK.

## 2. BACKGROUND

Star	$\dot{M}$ $M_{\odot} \text{ yr}^{-1}$	$v_{\infty}$ $\text{km s}^{-1}$	Mechanism
Sun	$10^{-14}$	400	Thermal heating
Pre Main Sequence	$10^{-4} - 10^{-7}$	200-500	Rotation & magnetic fields
Red Giant	$10^{-7} - 10^{-9}$	30	Radiation pressure on dust grains
OB Star	$10^{-7} - 10^{-8}$	2500	Radiation pressure & line driving
Wolf-Rayet	$10^{-5}$	1500	Radiation pressure & line driving

**Table 2.1:** Comparison winds emitted from various types of star.

### 2.2.3 The CAK formalism

## 2.3 Interstellar Dust

### 2.3.1 The importance of interstellar dust

### 2.3.2 Interstellar dust in massive star systems

## 2.4 Colliding Wind Binary Systems

Colliding Wind Binaries<sup>1</sup>, in opposition to all known laws of astrophysical nomenclature, is a easy to understand term - it is a binary system where stellar winds from the member stars undergoing collision. Unfortunately, the simplicity of the systems ends here, CWB systems are extremely complex and poorly understood as they are difficult environments to observe or simulate.

Early observations beyond visual spectrum led to the discovery of many new astrophysical phenomena, one such discovery were extremely bright persistent thermal x-ray sources, with x-ray The first classification and analysis of Colliding Wind Binary systems were independently performed by Prilutskii and Usov, 1976 and Cherepashchuk, 1976, these systems were found to contain a close binary system, consisting of an evolved WR star and an OB counterpart, as their winds collide, a strong shock forms, heating the winds to temperatures in the order of  $10^8$  K in the immediate post-shock environment, these extreme temperatures and the large quantity of shocked material accounted for the extremely bright thermal x-ray emission. The evidence was further compounded as the variation of the x-ray flux could be attributed to orbital motion of

---

<sup>1</sup>Abbreviated to CWBs.

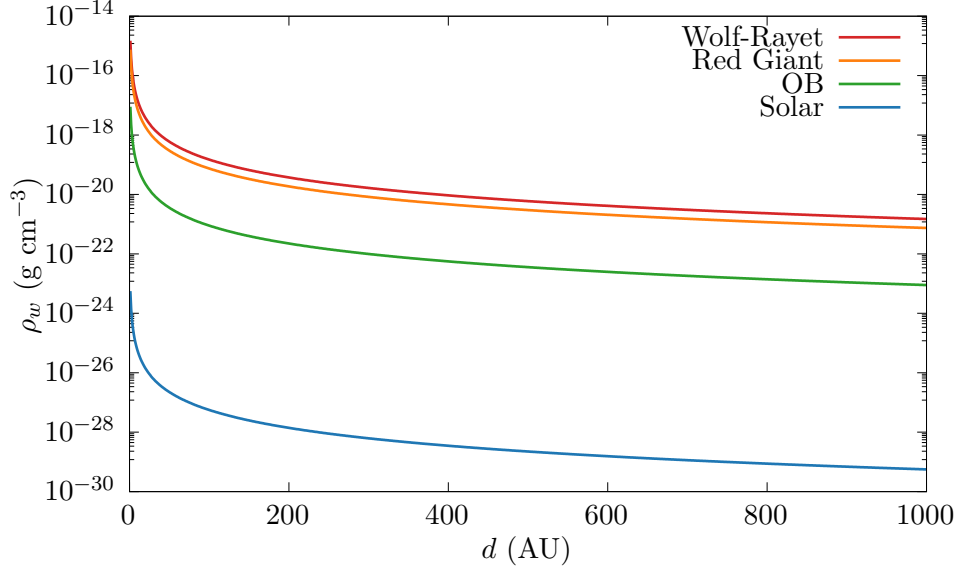


**Figure 2.3:** Comparison of the densities of various main sequence winds using the parameters specified in table 2.1, wind densities are estimated using the smooth wind approximation described in equation 2.6.

these binary systems.

### 2.4.1 The Wind Collision Region

The Wind Collision Region<sup>1</sup> is the most violent and turbulent region of a CWB system, a region where strong shocks lead to temperatures in excess of  $10^8$  K. These strong shocks contain enormous amounts of mechanical energy, in the region of  $10^3 L_{\odot}$ , WCRs are engines capable of producing huge quantities radiation through multiple thermal and non-thermal mechanisms (Eichler & Usov, 1993; Grimaldo et al., 2019). Despite these extreme conditions, these regions are capable of producing amorphous carbon dust grains at a rate on the order  $1 \times 10^{-8} M_{\odot} \text{ yr}^{-1}$ . As these grains are extremely fragile, this is a conundrum that has plagued researchers in this field, as direct observation of the innermost regions of even nearby WCRs is difficult, bordering on impossible, much of the work in this area involves hydrodynamical simulation.

The properties of the WCR can be described by a small number of parameters. The first of such parameters is the wind momentum ratio,  $\eta$ , which describes the available (Usov, 1991).

<sup>1</sup>WCR

## 2. BACKGROUND

---

$$\eta = \frac{\dot{M}_{\text{OB}} v_{\infty}^{\text{OB}}}{\dot{M}_{\text{WR}} v_{\infty}^{\text{WR}}}, \quad (2.8)$$

This momentum ratio can also be used to estimate the distance of the apex of the WCR to each star, using the following equations:

$$r_{\text{WR}} = \frac{1}{1 + \eta^{1/2}}, \quad r_{\text{OB}} = \frac{\eta^{1/2}}{1 + \eta^{1/2}}, \quad (2.9)$$

where  $r_{\text{WR}}$  is the distance from the WR star to the WCR apex, and  $r_{\text{OB}}$  is the distance from the OB star to the WCR apex. Work by Eichler and Usov, 1993 goes further to utilise the momentum ratio to approximate the shape of the wind collision region, further out from the apex of the WCR, the region forms an approximately conical shape with an opening angle,  $\theta_c$  of:

$$\theta_c \simeq 2.1 \left( 1 - \frac{\eta^{2/5}}{4} \right) \eta^{-1/3}, \quad \text{for } 10^{-4} \leq \eta \leq 1, \quad (2.10)$$

### 2.4.2 Cooling in the WCR

Temperature range	Dominant process	Spectral region
$5 \times 10^3 \text{ K} \lesssim T \lesssim 1 \times 10^5 \text{ K}$	Forbidden lines	IR, Optical
$T \approx 1 \times 10^5 \text{ K}$	H excitation/ionisation	Optical, UV
$5 \times 10^3 \text{ K} \lesssim T \lesssim 1 \times 10^5 \text{ K}$	Resonance lines	Far UV, soft X-ray
$T \gtrsim 1 \times 10^8 \text{ K}$	Bremsstrahlung	Radio

**Table 2.2:** Breakdown of dominant cooling processes at various temperature ranges from Dyson, 2021, whilst H excitation/ionisation occurs over a very short temperature range, it is extremely influential, causing a global peak in the cooling rate at  $\approx 10^5 \text{ K}$ . These temperature ranges are depicted in figure 2.4.

Cooling due to radiation emission in a hot plasma can be broken down into a variety of processes that occur over series of temperature ranges. Ions inside a plasma can be collisionally or photonically excited, resulting in emission through a variety of mechanisms.

Mechanisms that are significant within the warm<sup>1</sup> and hot gas phases include forbidden line emission, hydrogen excitation and ionisation, resonance lines and bremsstrahlung, the influence

---

<sup>1</sup>See what I mean about the phrase “warm”?

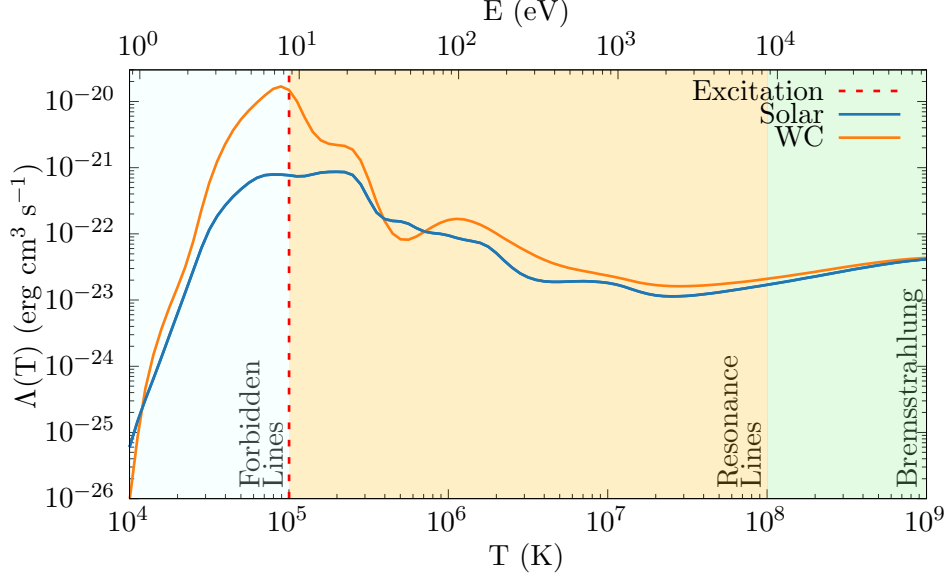


**Figure 2.4:** Normalised plasma cooling rates as a function of temperature and thermal energy for solar abundance and WC abundance winds. The regions where forbidden line, resonance line and bremsstrahlung emission are dominant are highlighted, with H ionisation and recombination occurring between the forbidden and resonance line sections at  $10^5$  K.

of each mechanism waxes and wanes as temperature increases, with each mechanism clearly dominant over (Dyson, 2021).

As the particle energy reaches the range of tens of keV, bremsstrahlung<sup>1</sup> becomes dominant (figure 2.4). High velocity electrons are deflected by ions, emitting radiation in the process due to conservation of energy.

(Schure et al., 2009) (Rybicki & Lightman, 2004)

$$\tau_{\text{cool}} = \frac{k_B T_s}{4n_w \Lambda(T_s)}, \quad (2.11a)$$

$$\tau_{\text{esc}} = \frac{d_{\text{sep}}}{c_s}, \quad (2.11b)$$

$$\chi = \frac{\tau_{\text{cool}}}{\tau_{\text{esc}}} \approx \frac{v_{\infty,8}^4 d_{\text{sep},12}}{\dot{M}_{-7}}, \quad (2.12)$$

The presence of dust within the immediate post-shock environment significantly increases the cooling rate. Figure 2.5 compares rate of cooling due to dust emission of various types of

<sup>1</sup>Or braking radiation when you can't remember how to spell it.

## 2. BACKGROUND

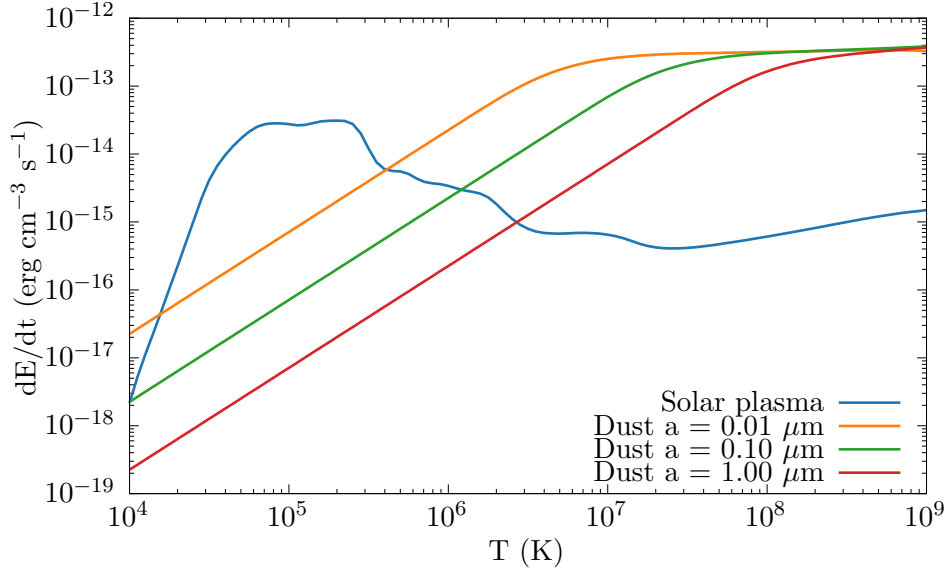


**Figure 2.5:** Comparison of plasma cooling to dust cooling with different grain sizes in a solar abundance gas, where  $\rho_g = 10^{-20} \text{ g cm}^{-3}$  and a dust-to-gas mass ratio of 0.01.

grains to plasma cooling at solar abundances, As  $\Lambda_g$  and  $\Lambda_D$  are both proportional to  $\rho_g^2$ , dust cooling will dominate at high temperatures so long as there is sufficient amounts of dust.

As dust grains collide with ionised gas and electrons, this imparts kinetic energy into the grains, heating them and causing them to emit infrared radiation. Assuming that there is a net accretion of ions and electrons onto the dust grains and the gas is optically thin in the infrared regime, energy is efficiently removed from the gas. At particularly high temperatures this effect can dominate over high-temperature plasma cooling processes such as bremsstrahlung, as seen in figure 2.5. Figure 2.6 compares dust grain heating rates due to electron and ion collisional excitation in a solar abundance and WC abundance flow. At lower temperatures the dust grain cooling rate is dominated by electron excitation, especially in the WC case as the ratio of free electrons to ions is significantly higher, as the WC flow is enriched by heavier elements. However, as the grain temperature increases, collisional heating due to ions becomes more prevalent as the electrons are sufficiently energetic to pass through the grain without significant energy transfer; this is referred to as the electron transparency,  $h_e$  (Dwek & Werner, 1981).

Work by Dwek and Werner, 1981 is used predominantly in this project to simulate cooling due to dust, a fast method for calculating the cooling rate due to dust was integrated into the numerical code for this project, which is elaborated on in section 3.6.2.

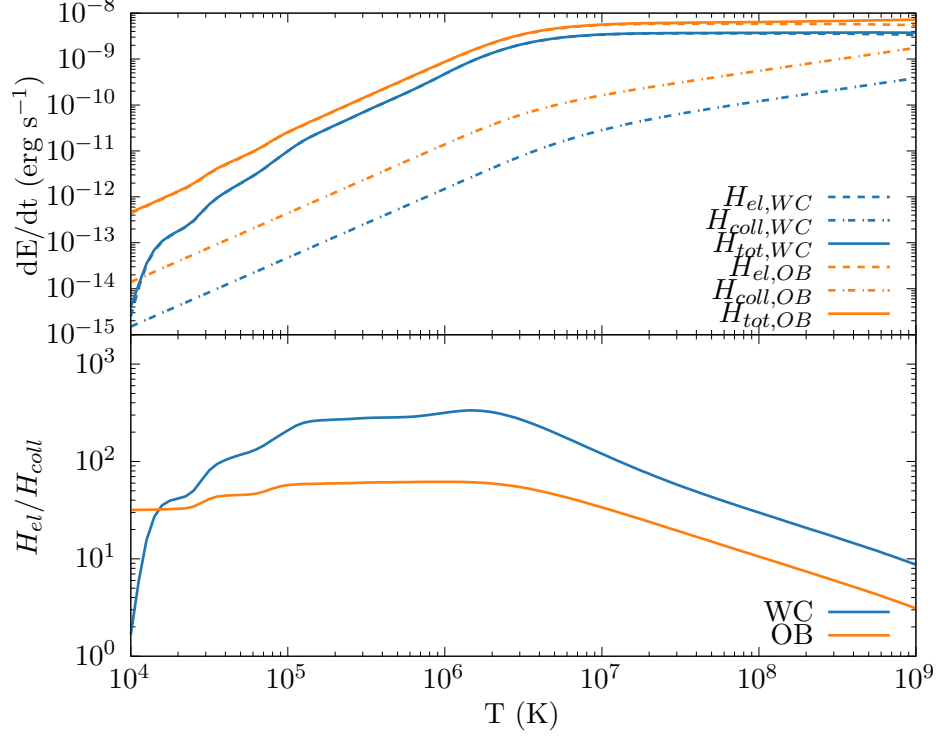


**Figure 2.6:** Comparison of grain heating rate due to ion collisional excitation,  $H_{coll}$ , and electron excitation,  $H_{el}$ . The dust grain has a grain radius of  $5 \times 10^{-3} \mu\text{m}$  and is travelling through a gas with a density of  $10^{-20} \text{ g cm}^{-3}$  with solar and WC abundances.

The heating rate of a dust grain due to collisions

$$H_{coll} = n\pi a^2 \langle Q(E, q, U) \rangle \times \langle v(E - qU) f(a, E - qU) f(a, E - qU) \rangle \text{ erg s}^{-1} \quad (2.13)$$

This can be simplified and expressed in the equation:

$$\begin{aligned} H_{coll} &= \left( \frac{32}{\pi m} \right)^{1/2} n\pi a^2 (k_B T)^{3/2} h(a, T) \\ &= 1.26 \times 10^{-19} \frac{n}{A^{1/2}} a^2 (\mu\text{m}) T^{3/2} h(a, T) \text{ erg s}^{-1} \end{aligned} \quad (2.14)$$



## 2. BACKGROUND

---

2.4.3 Dust formation in CWB systems

2.4.4 Important WCd systems

2.4.5 Contemporary research in extragalactic low-metallicity WCd systems

---

# CHAPTER 3

---

Methodology & Numerical Simulation

### 3. METHODOLOGY & NUMERICAL SIMULATION

---

#### 3.1 The Purpose of Numerical Simulations

#### 3.2 The Mathematics of Numerical Simulations

#### 3.3 Computational Hydrodynamics

#### 3.4 The Athena++ Hydrodynamical code

#### 3.5 Simulating CWB systems

##### 3.5.1 Assumptions

#### 3.6 Cooling in numerical simulations

##### 3.6.1 Plasma cooling

##### 3.6.2 Dust cooling

A particular difficulty in precisely calculating the rate of cooling due to emission from dust is calculating the electron transparency,  $h_e$ .<sup>1</sup>  $h_e$  can be computed via integration by parts, however due to this occurring in the main cooling loop, this results in a nesting of integrals, which can lead to extremely time-consuming computation for individual cells. Initial tests using the integral method within a numerical simulation led to severe slowdown as processing time for cooling took up to 90% of the overall processing time for each timestep.

Multiple options were considered for improving the performance of this routine. Initially, a  $\Lambda_d$  lookup table was considered, this consisted of a logarithmically spaced table of  $\rho$ ,  $a$ ,  $T$  and  $\Lambda_d$  values calculated by an implementation of the Dwek and Werner, 1981 prescription. A binary search for each parameter is performed, with the an offset being calculated for each parameter,

$$P_d = \frac{P - P_0}{P_1 - P_0}, \quad (3.1)$$

these offsets are then used to perform a trilinear interpolation to calculate  $\lambda_d$  from the lookup table.

---

<sup>1</sup>The probability that an electron will embed in the dust grain and heat it, rather than pass through.

$$\begin{aligned}
 \Lambda_{00} &= \Lambda_{000} (1 - \rho_d) + \Lambda_{100} \rho_d, \\
 \Lambda_{01} &= \Lambda_{001} (1 - \rho_d) + \Lambda_{101} \rho_d, \\
 \Lambda_{10} &= \Lambda_{010} (1 - \rho_d) + \Lambda_{110} \rho_d, \\
 \Lambda_{11} &= \Lambda_{011} (1 - \rho_d) + \Lambda_{111} \rho_d, \\
 \Lambda_0 &= \Lambda_{00} (1 - a_d) + \Lambda_{10} a_d, \\
 \Lambda_1 &= \Lambda_{01} (1 - a_d) + \Lambda_{11} a_d, \\
 \Lambda &= \Lambda_0 (1 - T_d) + \Lambda_1 T,
 \end{aligned} \tag{3.2}$$

where 0 is the lookup table value lower than the parameters actual value, and 1 is the lookup table value greater than the parameters actual value. This implementation was written in the form of a series of nested loops to utilise SIMD vectorisation to improve performance.

Whilst this method is significantly faster than calculating  $\Lambda$  for each cell with an integration step, a  $(100 \times 100 \times 100)$  lookup table requires approximately 32 MB of memory to store, and is much more time consuming to search through. As such, eliminating complexity from the binary search and reducing the number of interpolations were identified as improvements to the. These optimisations were made by simplifying the lookup table into a series of smaller lookup tables and relying on even logarithmic spacing of the lookup table to determine the parameter indices, rather than performing a binary search for them. Additionally, as  $\rho$  and  $a$  are invariant within the cooling loop, these parameter offsets are solved separately using a bilinear interpolation, while in the cooling sub-step loop, a separate linear offset is performed to find the temperature offset, solving to find  $\Lambda_d$ . These optimisations resulted in this method scaling significantly better, as there is a lower total number of calculations required as the number of sub-steps increases (figure 3.1).

The second method considered for solving the  $h_e$  integral was using an approximation described by Dwek and Werner, 1981 where  $h_e$  could be described by a series of equations:

$$\begin{aligned}
 h_e(x^*) &= 1, & x^* > 4.5, \\
 &= 0.37x^{*0.62}, & x^* > 1.5, \\
 &= 0.27x^{*1.50}, & \text{otherwise,}
 \end{aligned} \tag{3.3}$$

where  $x^* = 2.71 \times 10^8 a^{2/3} (\mu\text{m})/T$ . Whilst this is less accurate, especially in the region where one case ends and the other begins where the result begins to diverge, this method is multiple orders of magnitude faster. Figure 3.2 shows these discrepancies, in the case where electron

### 3. METHODOLOGY & NUMERICAL SIMULATION

---

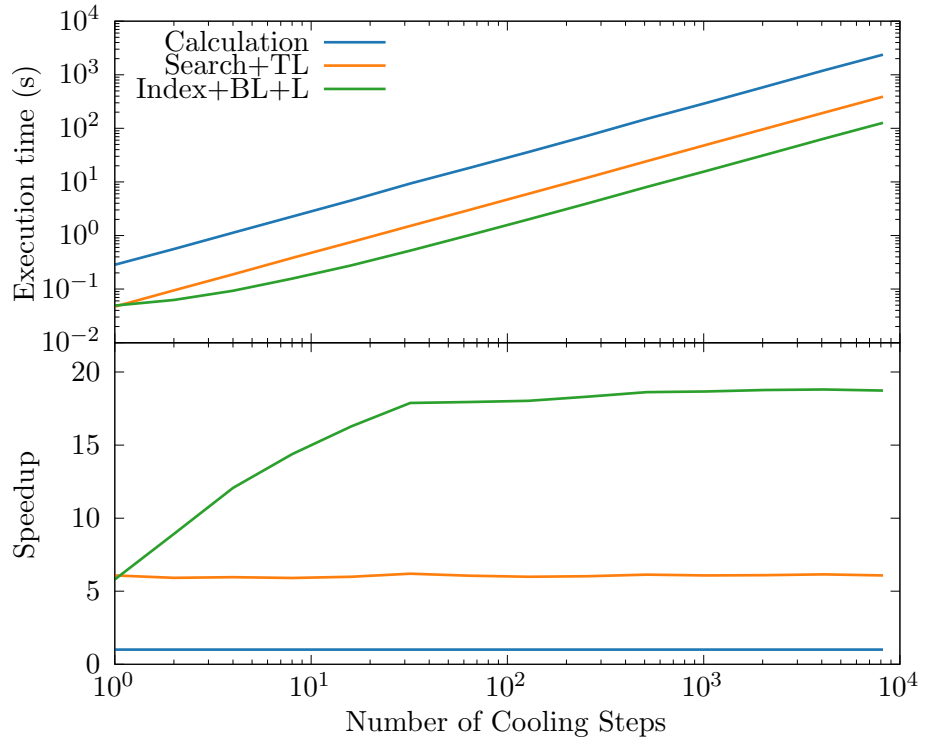


**Figure 3.1:** Comparison of execution time and speedup for lookup table methods.

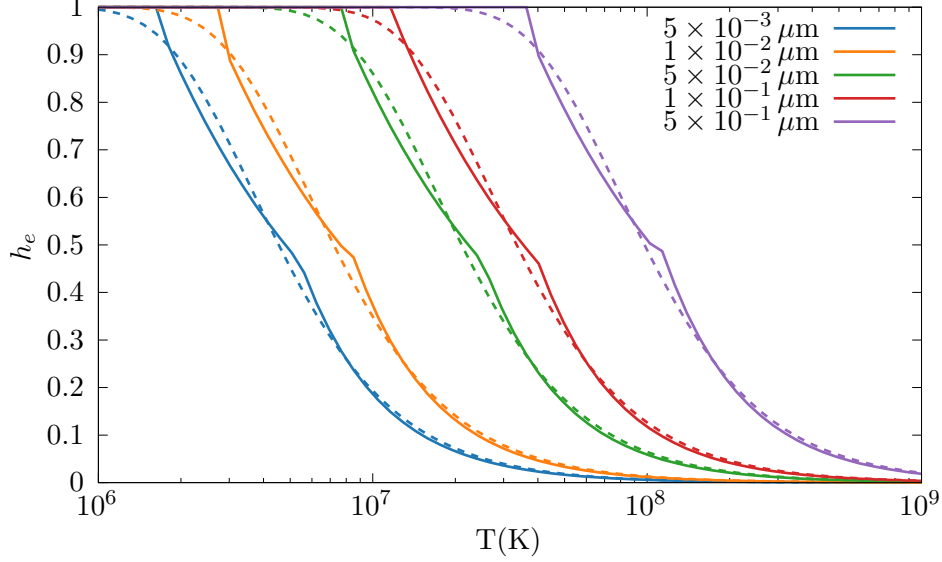


**Figure 3.2:** Grain transparency as a function of temperature for the estimate method described in equation 3.3 (solid lines) and a 400 bin integration method (dashed lines).

transparency begins to decrease the approximation is out somewhat significantly, as well as mid-way through the curve, whilst at temperatures below  $10^6$  K the approximation and integral methods are perfectly aligned. As the grains grow hotter and the electron transparency reduces, the influence on the cooling rate due to incident electrons reduces quite drastically, meaning that extremely high accuracy is less important at these temperatures (figure 3.3). The accuracy of the approximation method is also shown in figure 3.4, the estimated value for  $\Lambda_d$  closely matches the integrated value aside from the smallest dust grains at very high temperatures  $T > 6 \times 10^8$  K.

Table 3.1 shows the improvements to performance inherent in the estimation method; the final result is that the approximation is over 24,500% faster, the resulting dust cooling function therefore will have a minimal computational impact on the cooling loop as a whole. As this approximation was conclusively shown to not significantly effect the cooling rate due to grain heating, the approximation was chosen.

Further improvements were made to correctly determine the electron number,  $n_e$ , to calculate the cooling contribution for dust due to grain-electron collisions. the initial version of this code assumed that  $n_e = 1.1n_p$ , an estimate based on solar abundances, however the electron-to-ion ratio varies significantly with temperature in a WC wind, which is hydrogen depleted and as such can vary from 0 to  $\sim 4$  between  $1 \times 10^4$  and  $5 \times 10^6$  K (figure 3.5). In order to solve

### 3. METHODOLOGY & NUMERICAL SIMULATION

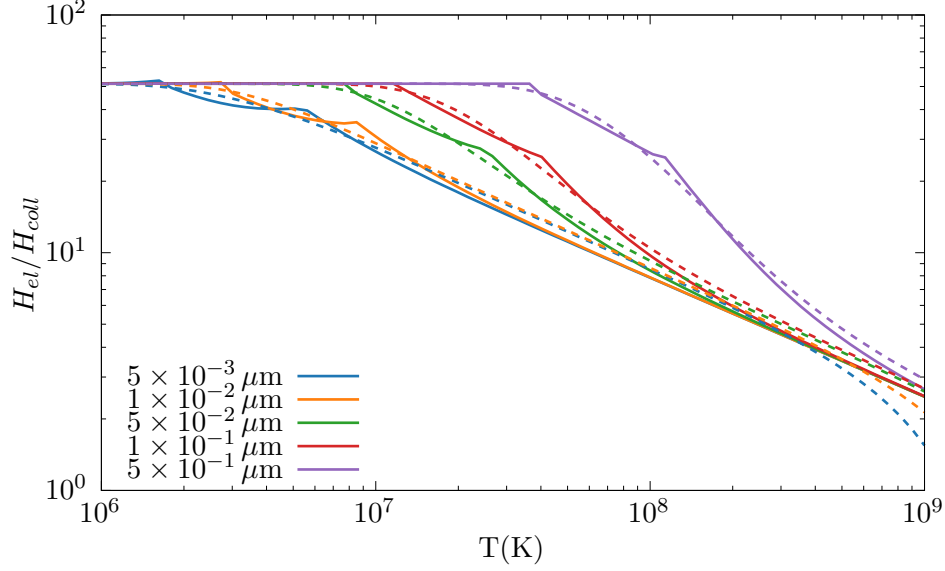


**Figure 3.3:** Comparison of the ratio heating rate of a dust grain due to incident electrons and incident atoms as a function of temperature for various grain sizes, whilst the result between the integration method and estimate method diverge, this is while the contribution of heating from electrons becomes less influential on the cooling rate of the grain.

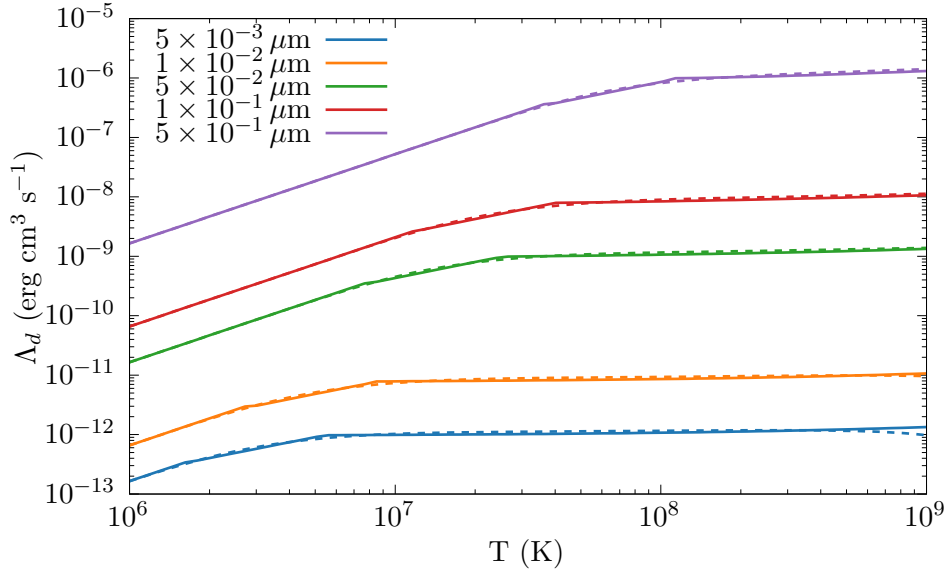


**Figure 3.4:**  $\Lambda_d$  as a function of temperature for various grain sizes, the estimate method is extremely close to the integral value aside from at the highest temperatures.

### 3.7 The BODMAS Advected Scalar Dust Model

Method	t(s)	Iter/s	Speedup
400 bin integration by parts	36.03	35,526	-
Binary search + trilinear	6.016	212,751	599%
Index calculation + bilinear + linear	1.999	640,447	1,803%
Dwek and Werner, 1981 approximation	0.147	8,693,171	24,510%

**Table 3.1:** Comparison of methods explored for estimating  $\Lambda_d(\rho, a, T)$  in cooling code,  $10^4$  initial values were chosen and 128 cooling sub-steps were performed, benchmark code was compiled and run using GCC 10.3.0 with the -O3 optimisation set on an Intel i7-7700HQ processor with a maximum clock speed of 3.8 GHz.

this problem quickly for each timestep, a lookup table similar to the plasma cooling curves was used, containing the electron-ion ratio at temperatures between  $10^4$  and  $10^8$  K for each wind abundance.

#### 3.6.3 Exact cooling method

### 3.7 The BODMAS Advected Scalar Dust Model

### 3.8 Contemporary Dust Models

#### 3.8.1 The Hendrix dust model

Perhaps the most similar contemporary dust model is the model described in Hendrix et al., 2016 - as this model is concerned with simulating the dynamics of dust within a CWB. This is not to say that these models are identical, of course, as the Hendrix model explores how dust spreads throughout the WCR of WR 98a, in order to compare with observational data using radiative transfer code.

The main differentiating factors between this model and our model are the driving mechanism and dust evolution. In the Hendrix model dust is modelled as a separate fluid, with an Epstein drag function between the wind and dust fluids; this method allows for dust kinematics that aren't implicitly co-moving. This is a more accurate method of modelling dust, however it requires significantly more processing time and is much more difficult to implement, requiring a numerical code that supports multiple fluids. At the start of this PhD this was considered but eventually rejected due to time constraints.



### 3. METHODOLOGY & NUMERICAL SIMULATION

---

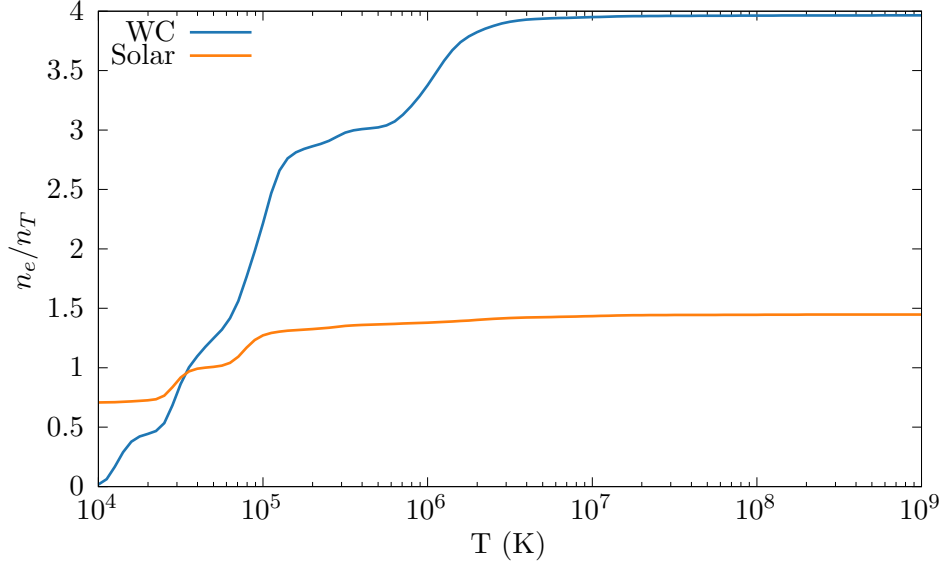


**Figure 3.5:** Ionisation fraction

The purpose of the Hendrix model is to analyse the distribution of dust within a CWB system, rather than to model the evolution of the dust itself. To this end, the Hendrix model does not

#### 3.9 Future dust models

The increased inertia of more massive dust grains could result in the kinematics of the dust flow diverging from the co-moving assumption. To that end, a successor dust model would adopt a multi-fluid and drag function method, which was considered but not included for the sake of time.

---

# CHAPTER 4

---

A Parameter Space Exploration of Dust Formation  
within WCd Systems Using an Advected Scalar Dust  
Model

## 4. A PARAMETER SPACE EXPLORATION OF DUST FORMATION

---

### Abstract

### 4.1 Introduction

A Wolf-Rayet star is known to be a hydrogen depleted OB-type star, as vigorous Triple- $\alpha$  fusion reactions within the core exert massive radiation pressures upon the stars envelope, driving it away in the form of a dense, fast ( $\sim 1000 \text{ km s}^{-1}$ ) wind. Through this mechanism, enormous mass-loss rates on the order  $10^{-5} \text{ M}_{\odot} \text{ yr}^{-1}$  are produced (Crowther, 2007). Wolf-Rayet stars have multiple subtypes, based on their elemental abundances, WC, which is Carbon abundant, WN, which is Nitrogen abundant, and WO, which is Oxygen abundant. These systems can also be divided into early and late type, depending on the level of Hydrogen depletion.

The WC subtype is of particular importance in this paper, due to its dust producing properties. Despite the extremely high UV flux and wind temperature of these stars ( $L_* \gtrsim 10^5 L_{\odot}$ ,  $T_* \gtrsim 40,000 \text{ K}$ ), interstellar dust in significant quantities has been observed in a number of systems. The presence of a binary partner - either OB or WR type - facilitates dust formation through colliding winds, which produce extremely high local densities and a UV-opaque medium conducive to dust formation. While a large proportion of WC stars are a part of a binary system systems that exhibit colliding wind properties are considerably rarer (Rosslove & Crowther, 2015). Despite this, the massive quantities of dust formed from these systems (between  $10^{-10}$  and  $10^{-6} \text{ M}_{\odot} \text{ yr}^{-1}$ ) can substantially affect the local interstellar medium (ISM).

CWB systems can be described using two important variables, the wind momentum ratio,  $\eta$  and the cooling parameter,  $\chi$ . The wind momentum ratio is fairly self-explanatory, describing how dominant the primary wind is over the secondary. In the case of a WR+OB pair, the WR star is invariably dominant, with the equation taking the form:

$$\eta = \frac{\dot{M}_{\text{OB}} v_{\text{OB}}^{\infty}}{\dot{M}_{\text{WR}} v_{\text{WR}}^{\infty}}, \quad (4.1)$$

where  $\dot{M}$  denotes the mass loss rate of a star, while  $v^{\infty}$  is the terminal velocity of a stars outflow. A low mass loss ratio indicates that the winds are extremely imbalanced, with one star dominating in terms of outflow. As momentum ratio decreases, the apex of wind collision region is pushed towards the secondary star, such that:

$$r_{\text{OB}} = \frac{\eta^{1/2}}{1 + \eta^{1/2}} d_{\text{sep}}, \quad (4.2)$$

where  $d_{\text{sep}}$  is the orbital separation of the binary pair. In the case of a very small wind momentum ratio the primary stars wind completely envelopes the secondary stars forming a strong shock front; the geometry of which can be approximated in the form of a conic surface with an opening angle,  $\theta$ ,

$$\theta \simeq 2.1 \left( 1 - \frac{\eta^{2/5}}{4} \right) \eta^{-1/3} \quad \text{for } 10^{-4} \leq \eta \leq 1, \quad (4.3)$$

to a high degree of accuracy (Eichler & Usov, 1993).

The cooling parameter,  $\chi$ , compares the cooling time to the escape time from the shock region for a parcel of gas in the immediate post-shock environment. An approximation can be made using the known parameters of a system using the equation:

$$\chi = \frac{t_{\text{cool}}}{t_{\text{esc}}} \approx \frac{v_8^4 d_{12}}{\dot{M}_{-7}}, \quad (4.4)$$

where  $v_8$  is the wind terminal velocity in units of  $10^8 \text{ cm s}^{-1}$ ,  $d_{12}$  is the distance to the WCR apex in units of  $10^{12} \text{ cm}$ , and  $\dot{M}_{-7}$  is the mass loss rate in units of  $10^{-7} \text{ M}_{\odot} \text{ yr}^{-1}$  (Stevens et al., 1992). Small values of  $\chi$  indicate that radiative cooling dominates the dynamics of the system, while larger values indicate an adiabatic system. Strong cooling occurs in comparatively slow, dense winds with a high metallicity, as such it can be predicted that the post-shock WR flow will rapidly cool from the immediate post-shock temperature of  $10^8 \text{ K}$  to temperatures in the dust formation range,  $\lesssim 10^4 \text{ K}$ .

Dust producing CWB systems have been observed forming dust either persistently or continuously, further observations have noted that systems with persistent dust formation have more circular orbits, while systems with

Furthermore, dust producing CWB systems are capable of forming dust both persistently or continuously. Observations of a variety of systems have determined that the dust formation periodicity appears to be dependent on the orbital properties of the system - dust is formed continuously in systems with more circular orbits while periodic dust formation occurs in highly elliptical systems. This suggests that there is a range of parameters that lead to stars producing the conditions necessary to produce dust, and that at certain separations, dust formation can occur.

## 4. A PARAMETER SPACE EXPLORATION OF DUST FORMATION

---

This paper examines the changes to the dust formation rates of a system as the parameters of the system change. In particular, the orbital properties of the system, the effect of simulated cooling on the system, and changes in the wind momentum ratio by varying mass loss rate. An ideal continuous dust forming WR+OB system is used as a baseline, periodic dust forming systems are beyond the scope of this paper.

### 4.2 Simulating CWB Systems

Our simulations were generated using the Athena++ hydrodynamical code, created by Stone et al., 2020, simulations are generated in 3D and the Euler equations of hydrodynamics are solved in the form:

$$\frac{\partial \rho}{\partial t} + \nabla \cdot (\rho \mathbf{u}) = 0, \quad (4.5a)$$

$$\frac{\partial \rho \mathbf{u}}{\partial t} + \nabla \cdot (\rho \mathbf{u} \mathbf{u} + P) = 0, \quad (4.5b)$$

$$\frac{\partial \rho \varepsilon}{\partial t} + \nabla \cdot [\mathbf{u} (\rho \varepsilon + P)] = \dot{E}_{cool}, \quad (4.5c)$$

where  $\varepsilon$  is the total specific energy,  $\varepsilon = \mathbf{u}^2/2 + e/\rho$ ,  $\rho$  is the mass density,  $e$  is the internal energy density,  $P$  is the gas pressure and  $\mathbf{u}$  is the gas velocity.  $\dot{E}_{cool}$  is the energy loss rate from the fluid due to gas and dust cooling, which is elaborated on in section 4.2.3.

For these simulations Athena++ has been configured to run using a piecewise linear method with either a 3<sup>rd</sup> order Runge-Kutta or 4<sup>th</sup> order Strong Stability Preserving Runge-Kutta time-integration method (Spiteri & Ruuth, 2002). The 3<sup>rd</sup> order method is significantly faster and more memory efficient than the 4<sup>th</sup> order method, so is used if the simulation permits. Athena++ was forked from the original repository and additional routines were written for a Colliding Wind Binary case. A function to produce a steady outflow from a small spherical region around a set of cartesian co-ordinates was incorporated to simulate the outflow of both stars, while a function to move these co-ordinates with each time-step was included to simulate orbital motion. Additionally, Athena++ was further modified to include an advected scalar dust model for simulating dust growth and destruction as well as a photon emission cooling model to approximate cooling for gas and dust particles within the fluid.

### 4.2.1 Mesh refinement

Simulating a CWB system is a complicated task due to the extremely large range in length scales required to correctly observe the simulation. The initial wind collision region cannot be abstracted into a generic outflow if orbits are to be considered, as the separation of the stars is extremely important to the evolution of the wind collision region. Furthermore, as grain growth occurs over a long time scale, the maximum length scale must be correspondingly large.

Static mesh refinement is used to improve the effective resolution of the simulation. The region around the orbits of the stars is refined to the maximum level, with the refinement level decreasing further out from the simulation. Simulation extent is determined by the maximally refined region around the stars, extent is doubled for every level between the coarsest and finest levels.

SMR is used instead of Adaptive Mesh Refinement as it has proven to be more reliable within Athena++, as it mitigates unintentional over-refinement and refinement and de-refinement of the same meshblock every time-step, referred to as “grid-thrashing”. Overall using SMR the simulations are much more numerically stable. As the bulk of the dynamics governing the long-term evolution of the model occur over a small distance from the apex of the WCR, much of the simulation can be run at a lower resolution without affecting the simulation outcome significantly.

### 4.2.2 Wind mapping and orbits

Stars are simulated by replacing the values for density,  $\rho_R$ , energy  $E_R$ , and momentum,  $p_R$  within a small region, this region is typically on the order of 10 cells in radius. This rewrite corresponds to a change in mass and mechanical energy imparted by an outflowing wind, such that:

$$\rho_R = \frac{\dot{M}}{(4\pi r^2 v_\infty)} \quad (4.6a)$$

$$P_R = \frac{\rho_R}{\mu m_H} k_B T_w \quad (4.6b)$$

$$E_R = \frac{P_R}{\gamma - 1} + \frac{1}{2} \rho_R v_R^2 \quad (4.6c)$$

$$p_R = \rho_R v_R \quad (4.6d)$$

where  $v_R$  is the wind velocity as it flows radially from the center of the “remap zone” and  $r$  is the distance from the current cell to the centre of the remap zone. This method produces

## 4. A PARAMETER SPACE EXPLORATION OF DUST FORMATION

---

radially outflowing winds from the “star” with an expected density and velocity, whilst being stable against numerical error. Unrealistic behavior can occur if the WCR impinges on remap zone if the wind is extremely momentum imbalanced, this can be solved by increasing the simulation resolution.

Orbits are calculated by moving the remap zones over time, this is performed by calculating the current position of the zones using Kepler’s laws, this is simple, and makes orbits behave extremely consistently. In order to calculate these orbits, the orbital period, eccentricity and stellar masses are required in the input file.

### 4.2.3 Gas and dust cooling

Cooling due to photon emission from gas molecules and dust particles is simulated by removing energy from a cell at each timestep. This energy loss is calculated by integrating the energy loss rates using the Euler method; in regions with very rapid cooling sub-stepping is used to ensure that the solution is accurate, the number of sub-steps is determined by comparing the timestep to the cooling time of the region.

Gas cooling is simulated using a lookup table method, the table contains the gas temperature and associated emissivity,  $\Lambda(T)$  of the wind at that temperature. In a typical cooling step, the temperature is calculated and a binary search is performed to find the nearest temperature in the lookup table, a linear interpolation step is then performed to find an appropriate value for  $\Lambda$ . The emissivity is normalised for a  $1\text{cm}^{-3}$  volume with a density of  $1\text{g cm}^{-3}$ , as such, the energy loss can be calculated with the formulae:

$$\frac{dE}{dt} = \left( \frac{\rho}{m_H} \right)^2 \Lambda_w(T), \quad (4.7)$$

where  $\rho$  is the gas density and  $m_H$  is the mass of a hydrogen atom. The lookup table was generated by mixing a series of cooling curves generated by MEKAL from the properties of various pure elemental gasses, these are combined based on the elemental abundances of each wind such that:

$$\Lambda(T) = n_e n_i \sum X(E) \Lambda_E(T), \quad (4.8)$$

where  $n_e$  and  $n_i$  are the electron and ion number density of an element,  $X(E)$  is the abundance of an element, while  $\Lambda_E(T)$  is the cooling parameter of an element. Figure 4.1 details the emissivities of the cooling curves at various temperatures, as well as non-normalised emissivities for each element. Two lookup tables are used in the simulations, based on the elemental

abundances of each star. the Wolf-Rayet star uses a WC curve with a high carbon abundance and hydrogen depletion, while the OB star uses solar abundances. The abundances used in this projects simulations are presented in table 4.1.

	X(E)	
	Solar	WC
H	0.705	0.0
He	0.275	0.546
C	$3.07 \times 10^{-3}$	0.4
N	$1.11 \times 10^{-3}$	0.0
O	$9.60 \times 10^{-3}$	0.05
Ne	$1.75 \times 10^{-3}$	0.0
Na	$3.47 \times 10^{-5}$	$3.47 \times 10^{-5}$
Mg	$7.10 \times 10^{-4}$	$7.10 \times 10^{-4}$
Al	$6.13 \times 10^{-5}$	$6.13 \times 10^{-5}$
Si	$8.60 \times 10^{-4}$	$8.60 \times 10^{-4}$
S	$3.82 \times 10^{-4}$	$3.82 \times 10^{-4}$
Ar	$1.01 \times 10^{-4}$	$1.01 \times 10^{-4}$
Ca	$6.15 \times 10^{-5}$	$6.15 \times 10^{-5}$
Fe	$1.52 \times 10^{-3}$	$1.52 \times 10^{-3}$
Ni	$7.65 \times 10^{-5}$	$7.65 \times 10^{-5}$

**Table 4.1:** Abundances used for OB and WC stars

The cooling regime of this code ranges from  $10^4$  to  $10^9$ K, cooling or heating above or below these temperatures are automatically restricted.

A model for cooling due to emission from dust grains is also included. The rate of cooling is calculated using the uncharged particle case of the prescription described by Dwek and Werner, 1981. The cooling code simulates grains that are heated due to collisions with ions and electrons, with energy being immediately lost from the simulation as radiation. This assumes that infrared emission due to collisional heating is shorter than the cooling timestep, and the region being simulated is optically thin to far infrared photons. Ions are calculated by element by estimating their number density, and added to the total cooling rate, such that:



#### 4. A PARAMETER SPACE EXPLORATION OF DUST FORMATION

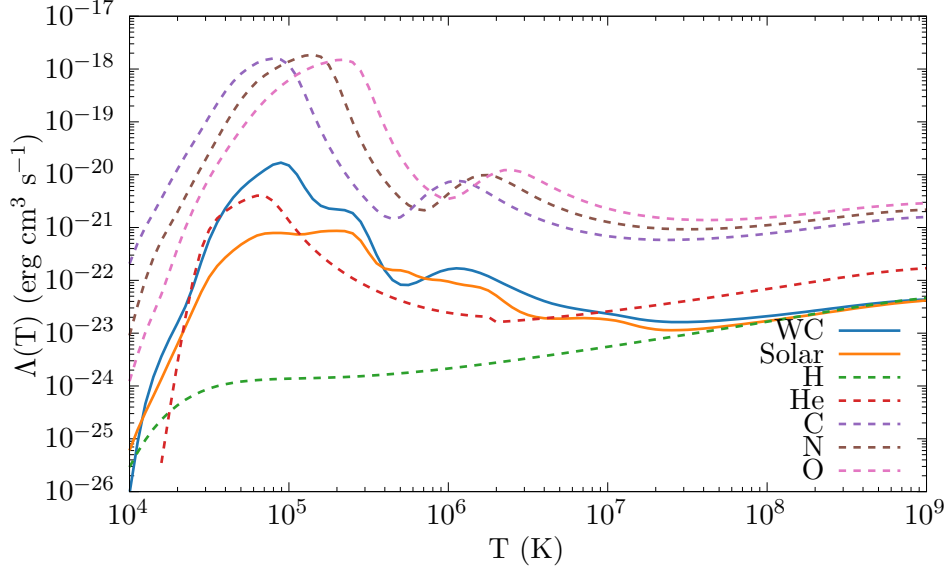


**Figure 4.1:** Comparison of lookup tables for calculating energy loss due to gas cooling, pure elemental cooling curves from MEKAL have been provided for the more abundant elements.

$$H_{\text{coll}} = 1.26 \times 10^{-19} \frac{n}{A^{1/2}} a^2 (\mu\text{m}) T^{3/2} h(a, T), \quad (4.9a)$$

$$\Lambda_d = \frac{H_{\text{coll}} + H_{\text{el}}}{n_H}, \quad (4.9b)$$

$$\frac{dE}{dt} = n_T n_d \Lambda_d, \quad (4.9c)$$

where  $H_{\text{coll}}$  is the heating rate due to atom and ion collisions,  $H_{\text{el}}$  is the heating rate due to electron collisions,  $h(a, T)$  is the particle transparency and  $n_T$  is the total number density.  $H_{\text{coll}}$  is summated for Hydrogen, Helium, Carbon, Nitrogen and Oxygen atom collisions. Other elements are not considered as they are present in trivial proportions in both winds.

Electron-grain collisions are modelled similarly to ions, with some differences. In particular, the electron number density needs to be accurately calculated, this is performed with a second series of lookup tables that contain the electron-to-ion ratio of each wind across a temperature range of  $10^4$  to  $10^9$  K (figure 4.4). Additionally, calculating electron transparency is a significantly more complex problem than ion transparency. Electron transparency is calculated via an approximation rather than an integration step, this is used to improve performance, as a time-consuming integration would have to be performed at each cooling substep. The approximation itself is derived from Dwek and Werner, 1981. The approximation for  $h(a, T)$  is:

$$\begin{aligned}
h(x^*) &= 1, & x^* > 4.5, \\
&= 0.37x^{*0.62}, & x^* > 1.5, \\
&= 0.27x^{*1.50}, & \text{otherwise,}
\end{aligned}
\tag{4.10}$$

where  $x^* = 2.71 \times 10^8 a^{2/3}(\mu\text{m})/T$ , this approximation makes the entire dust cooling calculation about 3000% faster than using a 400 bin integration<sup>1</sup>. Figures 4.2 and 4.3 compare each method, but at high temperatures maximum deviation of the approximation is on the order of 10%.

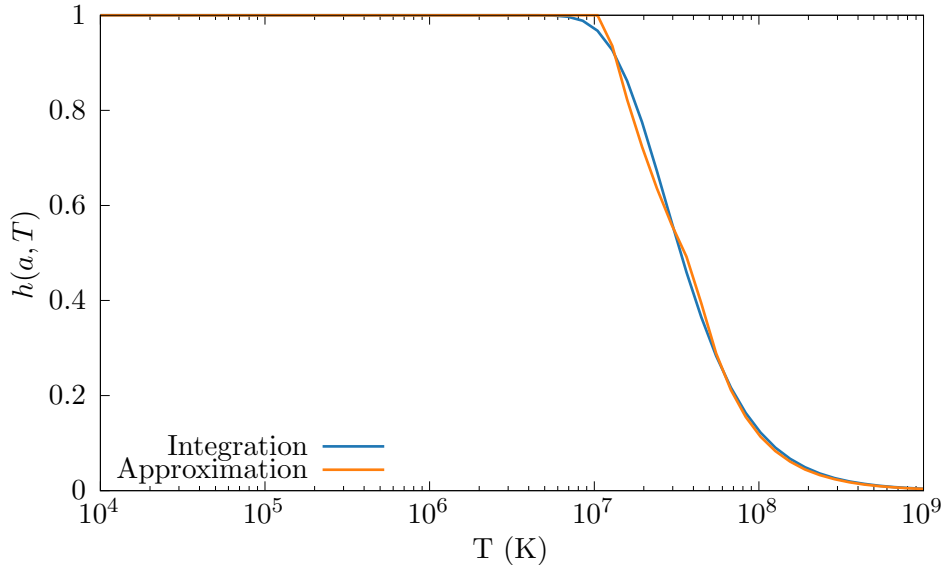


**Figure 4.2:** Comparison of  $h_e$  integration and approximation for increasing gas temperature, it is clear that the divergence between integration and approximation is at its largest at very high temperatures.

Grain-grain collision is not modelled, as this would be difficult to calculate due to the single-fluid model in use, further simulations utilising a multi-fluid model could allow for this to be simulated.

#### 4.2.4 Numerical modelling of dust through advected scalars

For this paper a simple dust growth and destruction model was utilised in order to simulate the production of dust within the WCR. Typically a multi-fluid model would be used with a

<sup>1</sup>The fastest still reasonably accurate integration.

#### 4. A PARAMETER SPACE EXPLORATION OF DUST FORMATION

---

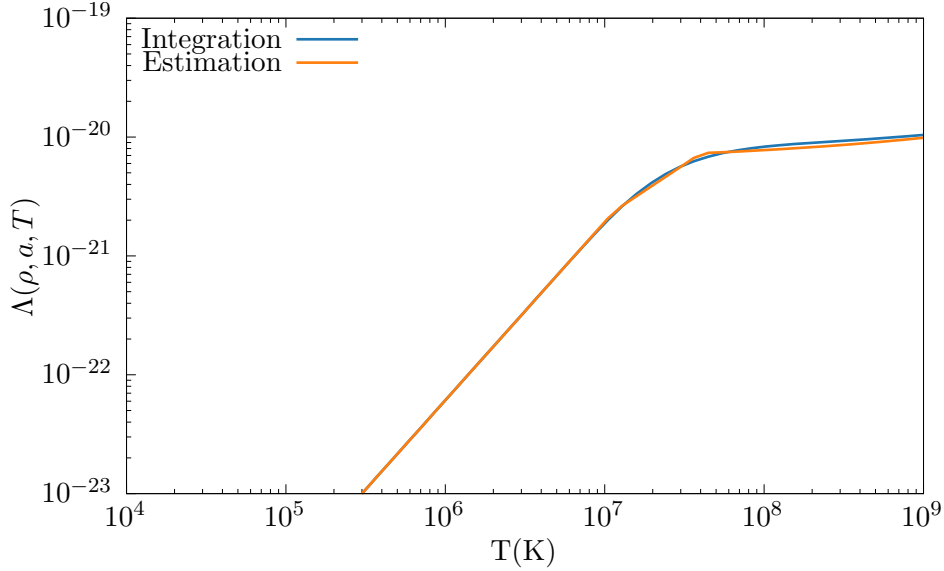


**Figure 4.3:** Comparison of dust cooling parameter  $\Lambda(T)$ . Error due to approximation does not propagate significantly to the calculation of  $\Lambda$  even at high temperatures.

coupling force between the gas fluid and the dust fluid; in this case, however dust is simulated in the form of a set of scalars, which advect according to the fluid dynamics laws governing the simulation. This method emulates the concept of a co-moving fluid, which previous papers have noted is an accurate dynamical model for dust within the WCR (Hendrix et al., 2016). In these simulations, dust is stored in the form of two constants, the average grain radius,  $a$ , and the dust-to-gas mass ratio,  $z$ . From these constants the dust production rate, number density, and total dust mass can be derived.

Additionally, a co-moving model allows for a simplified model of dust formation. In such a model, the mean particle velocity between two particles of different size can be given as:

$$\langle u \rangle = \left[ \frac{8kT}{\pi m_r} \right]^{1/2}, \quad (4.11)$$

where  $m_r$  is the familiar reduced mass between a test particle of mass  $m_t$  and a field particle of mass  $m_f$

$$m_r = \frac{m_f m_t}{m_f + m_t}. \quad (4.12)$$

As the dust grain is significantly more massive, the reduced mass is approximately equal to the grain mass, simplifying the dynamics of the simulation in a co-moving case (Spitzer Jr.,

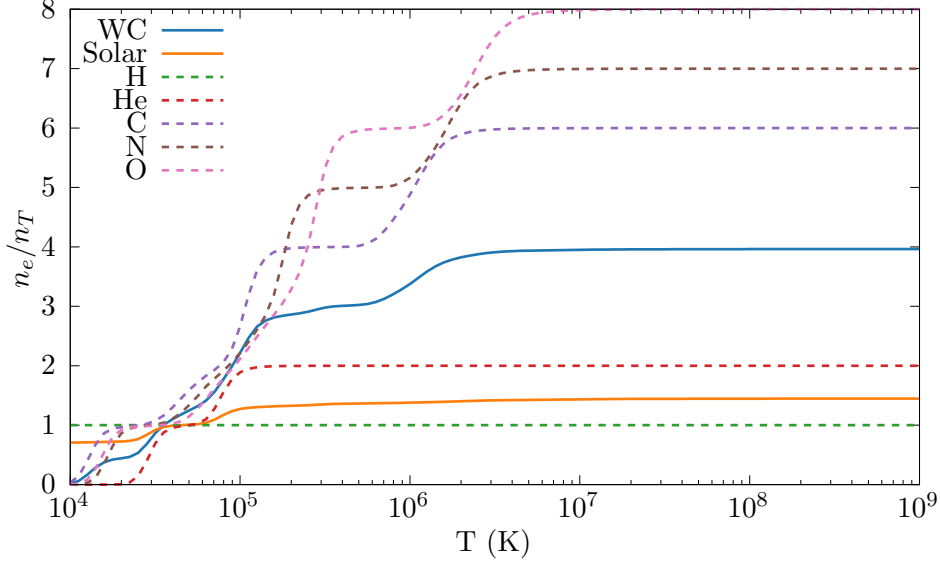


**Figure 4.4:** A comparison of the electron-ion ratio of both winds as temperature changes, included are the pure wind flows that the lookup tables are built from.

2008).

Dust growth is modelled through the method described by Spitzer Jr., 2008, grains co-moving with a gas perform low-velocity<sup>1</sup> collisions with the surrounding gas, accreting this gas onto the surface of the dust grain. Assuming a single average grain size and grains the change in average grain radius and total dust mass density

$$\frac{da}{dt} = \frac{\xi_a \rho_{Gr} w_a}{4\rho}, \quad (4.13a)$$

$$\frac{\rho_D}{dt} = 4\pi a^2 \rho n_D \frac{da}{dt}, \quad (4.13b)$$

where  $w_a$  is the Maxwell-Boltzmann distribution RMS velocity,  $\xi_a$  is the grain sticking efficiency,  $\rho_{Gr}$  is the grain bulk density,  $\rho$  is the gas density,  $a$  is the dust grain radius, and  $n_D$  is the grain number density. In this experiment,  $\xi_a$  is assumed to be 10%, while a bulk density analogous to amorphous carbon grains of  $3.0 \text{ g cm}^{-3}$  is used.

Dust destruction is calculated via gas-grain sputtering using the Draine & Salpeter prescription - a dust grain has a lifespan,  $\tau$ , which is dependent on the grain radius, as the grain loses

<sup>1</sup>Relative to the overall wind velocity

#### 4. A PARAMETER SPACE EXPLORATION OF DUST FORMATION

---

radius proportional to its loss in mass; assuming a spherical grain, the rate of change in mass and radius can be calculated such that:

$$\tau_D = 1 \text{ Myr} \times \frac{a}{n_g}, \quad (4.14a)$$

$$\frac{da}{dt} = -\frac{a}{\tau_D}, \quad (4.14b)$$

$$\frac{dm}{dt} = -1.33 \times 10^{-13} a^2 n_g n_d \rho_{Gr}, \quad (4.14c)$$

where  $n_g$  is the gas number density (Draine & Salpeter, 1979). More in-depth derivations for these equations can be found in the appendix, section ??.

In order to propagate dust through each simulation, a small initial value for the advected scalars is propagated from the remap zones, the grain radius was set to a sensible minimum grain size of  $50 \text{ \AA}$  while the minimum dust-to-gas mass ratio was set to  $10^{-6}$ , changing  $z_{min}$  does not significantly impact the average final dust-to-gas mass ratio of the system as  $z$  rapidly increases within the WCR, and only impacts the amount of dust formed outside of the WCR.

### 4.3 Model Parameters

For this project, a series of simulations were run in order to determine how dust formation varies due changes in orbital separation and wind momentum ratio. A baseline simulation with properties similar to WR98a was created, which is then modified to change either the orbital separation or wind momentum. Orbital separation is modified by changing the orbital period of the simulation, while wind momentum ratio is modified by adjusting the mass loss ratio and wind terminal velocity for each star. For all simulations a common wind temperature of  $1 \times 10^4 \text{ K}$  is utilised.

Parameter	WR	OB	Unit
$M$	10.0	10.0	$M_\odot$
$\dot{M}$	$5.0 \times 10^{-6}$	$5.0 \times 10^{-8}$	$M_\odot \text{ yr}^{-1}$
$v_\infty$	$1 \times 10^8$	$2 \times 10^8$	$\text{cm s}^{-1}$
$T_w$	$1 \times 10^4$	$1 \times 10^4$	K

**Table 4.2:** Wind properties of the baseline system

Parameter	Value	Unit
$d_{sep}$	$5.984 \times 10^{13}$	cm
$P$	$5.64 \times 10^7$	s
$e$	0.0	

**Table 4.3:** Baseline system orbital properties

#### 4.3.1 Cooling

For this experiment, 3 different simulations were run against each other in order to determine the influence of cooling changes the evolution of the system. All systems in this section have the same parameters, that of the baseline system described in tables 4.2 & 4.3, the parameter being varied was that of the presence of cooling, one simulation models cooling due to plasma and dust emission, another models cooling due to plasma emission only, whilst the final model does not simulate cooling at all, behaving completely adiabatically.

#### 4.3.2 Wind momentum ratio

Two sets of simulations were run which varied the wind momentum ratio, the first set of simulations varied  $\eta$  by modifying the mass loss rate of each star, while the second set of simulations adjusted the wind terminal velocity of each star. Each set of simulations had each parameter adjusted for both the Wolf-Rayet and OB star, this led to a total of 9 simulations, which are described in table 4.4.

Multiple simulations have similar momentum ratios and cooling parameters, but accomplished via different means, such as changing the secondary star wind rather than the primary. This is done in order to determine whether dust production changes are solely due to these two parameters.

#### 4.3.3 Separation distance

Another series of simulations was performed with a binary pair utilising wind parameters described in table 4.2 with a differing orbital separation. Separation was modified by changing the orbital period of each star; in this series, orbital separation was varied from 4 AU to 64 AU (table 4.5). The main effect of adjusting the orbital radius is the subsequent modification of the cooling parameter,  $\chi$ , which is inversely proportional to the separation distance. As such, the

#### 4. A PARAMETER SPACE EXPLORATION OF DUST FORMATION

$\dot{M}_{WR}$ $M_{\odot} \text{ yr}^{-1}$	$\dot{M}_{OB}$ $M_{\odot} \text{ yr}^{-1}$	$v_{WR}^{\infty}$ $\text{cm s}^{-1}$	$v_{OB}^{\infty}$ $\text{cm s}^{-1}$	$\eta$	$\chi_{WR}$
<i>Baseline</i>					
$5 \times 10^{-6}$	$5 \times 10^{-8}$	$1 \times 10^8$	$2 \times 10^8$	0.02	1.049
<i><math>\dot{M}</math> adjusted</i>					
$1.0 \times 10^{-5}$	$5.0 \times 10^{-8}$	$1 \times 10^8$	$2 \times 10^8$	0.01	0.544
$2.5 \times 10^{-6}$	$5.0 \times 10^{-8}$	$1 \times 10^8$	$2 \times 10^8$	0.04	1.995
$5.0 \times 10^{-6}$	$1.0 \times 10^{-7}$	$1 \times 10^8$	$2 \times 10^8$	0.04	0.997
$5.0 \times 10^{-6}$	$2.5 \times 10^{-8}$	$1 \times 10^8$	$2 \times 10^8$	0.01	1.088
<i><math>v^{\infty}</math> adjusted</i>					
$5 \times 10^{-6}$	$5 \times 10^{-8}$	$2 \times 10^8$	$2 \times 10^8$	0.01	17.41
$5 \times 10^{-6}$	$5 \times 10^{-8}$	$5 \times 10^7$	$2 \times 10^8$	0.04	0.062
$5 \times 10^{-6}$	$5 \times 10^{-8}$	$1 \times 10^8$	$4 \times 10^8$	0.04	0.997
$5 \times 10^{-6}$	$5 \times 10^{-8}$	$1 \times 10^8$	$1 \times 10^8$	0.01	1.088

**Table 4.4:** Momentum ratio modification parameters

purpose of these simulations is to confirm that dust formation rate relies strongly on  $\chi$ , or if there are other factors involved in dust formation.

Each simulation has a coarse resolution of  $320 \times 320 \times 40$  cells, with a varying number of levels, as the separation distance is doubled, the associated static mesh refinement box is halved and the number of levels is decremented. This manipulation of levels ensures that the number of cells between the stars is kept consistent, reduces memory usage and keeps the average timestep approximately the same.

P	$d_{sep}$	$\chi_{WR}$	Levels	Effective Resolution
s	AU			Cells
$5.647 \times 10^7$	4	1.049	7	$20480 \times 20480 \times 2560$
$1.597 \times 10^8$	8	2.097	6	$10240 \times 10240 \times 1280$
$4.518 \times 10^8$	16	4.194	5	$5120 \times 5120 \times 640$
$1.278 \times 10^9$	32	8.388	4	$2560 \times 2560 \times 320$
$3.614 \times 10^9$	64	16.78	3	$1280 \times 1280 \times 160$

**Table 4.5:** Parameters of simulations varying separation distance.

## 4.4 Momentum ratio variation

## 4.5 Separation variation

### 4.5.1 Adiabatic flow

### 4.5.2 Dust production yields

A clear trend with orbital separation is that dust formation increases drastically as the stars are positioned closer together, at high degrees of separation dust formation ceases, and average grain size drops below the initial value of  $50\text{\AA}$ .

The bulk of dust growth occurs in the immediate post shock region, as dust is rapidly cooled and at a high enough density for dust formation to occur.

This matches observations of episodic dust forming systems, where infrared emission due to dust is maximised at or shortly after periastron passage. This also lends further evidence that dust formation rates are not influenced solely by the momentum ratio, as this is kept constant, and instead is strongly influenced by the wind density at collision and post-shock cooling.

### 4.5.3 Periodicity within a circular orbit

Closer orbits were also observed to cause subtle periodic changes, whilst this effect is less pronounced than in a highly eccentric system, the

### 4.5.4 Wind mixing within the WCR

While interaction between Hydrogen and dust grains is not simulated by the dust model, Le Teuff, 2002 notes that Hydrogen could be a potential catalyst for amorphous carbon grain



#### 4. A PARAMETER SPACE EXPLORATION OF DUST FORMATION

---

formation.

---

# CHAPTER 5

---

Hydrodynamical Simulations of WCd Systems with an  
Advectioned Scalar Dust Model

### Abstract

### 5.1 Introduction

Wolf-Rayet (WR) stars are evolved massive stars that consist of a hydrogen-depleted envelope and a highly radiative core, these stars are so luminous that the total emission from their cores is greater than the Eddington Limit, causing the envelope to be removed from the star in the form of a fast, dense stellar wind. Whilst these stars have wind velocities comparative to their less evolved and massive OB counterparts ( $\sim 10^3 \text{ km s}^{-1}$ ) the mass-loss rate of these systems is many orders of magnitude larger ( $\sim 10^{-5} \text{ M}_{\odot} \text{ yr}^{-1}$ ).

As a majority of massive stars form in binary pairs, this can result in the fast, dense stellar wind of the WR component of the binary pair colliding with a significantly weaker stellar wind from its OB partner. This phenomena is referred to as a Colliding Wind Binary system if said phenomena plays an important role in the dynamics of the system. Observations of some of these systems have detected infrared excesses within the Wind Collision Region (WCR) which correspond with the emission from amorphous carbon dust grains. This is interesting as dust would be readily destroyed by evaporation via UV photons in the general medium, as well as the high gas temperature in the region. Instead it is believed that dust grows within the post-shock region, which rapidly cools due to the extremely high post-shock gas density. This high density region can also shield the nascent dust grains from the bulk of the photon flux from the binary stars, resulting in an ideal region for dust formation. Furthermore, this is only observed in systems where the primary star in the binary pair is a highly evolved WC9 star, this adds further complexity to the dust production problem as hydrogen depletion renders many formulation mechanisms dependent on hydrogen seeding impossible, reducing the potential yield of dust (Crowther, 2003; Williams, 2008).

Dust forming CWB systems<sup>1</sup> can produce upwards of  $10^{-8} \text{ M}_{\odot} \text{ yr}^{-1}$  of amorphous carbon dust, primarily in small grains  $\sim 100 \text{ \AA}$  in radius. This can have a significant impact on the local interstellar environment in the same manner that a dust producing Asymptotic Giant Branch star can impact its surroundings. CWBd systems can be further subdivided into two types of

---

<sup>1</sup>Referred to as WCd systems

system based on their dust emission based on their dust emission rates over time, persistently forming systems and episodically forming systems<sup>1</sup>. Based on the observations of various WCd and WCde systems there is a strong correlation between orbital eccentricity and dust production periodicity - dust forms readily at or after periastron pass, with dust production being reduced by multiple orders of magnitude at apastron (Williams & van der Hucht, 2015).

Whilst observational data of CWBd systems does exist, and dust formation can be readily observed, the distances from Earth to these systems, combined with the high levels of extinction due to the surrounding stellar wind result in it difficult to observe the dynamics of dust formation within the WCR. Instead numerical simulation of dust growth can be performed in order to discern how dust evolves in the system, this can then be compared to observations using radiative transfer modelling of the resultant numerical grids.

## 5.2 Methodology

Three systems were investigated for this paper, the persistent dust forming systems WR 98a and WR 104, as well as the periodic dust forming system WR 140. These systems were chosen as they have been previously been written about, and are considered archetypal dust producing CWB systems. The investigation consists of hydrodynamical modelling of the systems utilising a fork of the Athena++ hydrodynamical code, with modifications to the system in order to simulate binary system orbits, outflows and dust evolution Stone et al., 2020. Afterwards, the numerical grids produced by Athena++ are introduced into CONTINUE WHEN YOU HAVE MORE INFO ABOUT THIS

### 5.2.1 Hydrodynamics

### 5.2.2 Dust model and cooling

The dust model in this paper simulates dust growth and destruction through collisions between carbon atoms and dust grains. These grains are simulated in the form of advected scalars in each cell in the numerical grid which propagate with the same hydrodynamical rules as the stellar wind; as such dust can be described as co-moving with the interstellar wind. The two scalars in use are  $z$ , the dust-to-gas mass ratio within the cell, and  $a$ , the average grain radius. Using these parameters in addition to the local wind parameters, the dust can be adequately described and evolved with time.

---

<sup>1</sup>WCd

## 5. HYDRODYNAMICAL SIMULATIONS OF WCD SYSTEMS

---

A number of assumptions are made in this dust model, for instance, the dust grains are assumed to be spherical, with a uniform density of  $3 \text{ g cm}^{-3}$ . Dust grains are assumed to have a single size in a region, as well as a constant number density, as such, this model does not simulate grain agglomeration and fracturing. Additional mechanisms for dust formation and destruction could also be implemented such as grain-grain agglomeration and photoevaporation. Furthermore, a multi-fluid model with drag force coupling could also be implemented, however this is beyond the scope of this paper.

Dust is grown through grain accretion using formulae described by (Spitzer Jr., 2008). Dust grains grow via collisions with the surrounding gas, as gas accretes onto these grains the associated density is subtracted from the gas density, and added to the

$$\frac{da}{dt} = \frac{\xi_a \rho_{Gr} w_a}{4\rho}, \quad (5.1a)$$

$$\frac{\rho_D}{dt} = 4\pi a^2 \rho n_D \frac{da}{dt}, \quad (5.1b)$$

where  $w_a$  is the Maxwell-Boltzmann distribution RMS velocity,  $\xi_a$  is the grain sticking efficiency,  $\rho_{Gr}$  is the grain bulk density,  $\rho$  is the gas density,  $a$  is the dust grain radius, and  $n_D$  is the grain number density. For these simulations, the grain sticking factor has been set to 10%, while for low temperature collisions a sticking factor of 100% can be proven, grain sticking in a more energetic, hot regime could significantly reduce the probability of sticking.

Dust destruction is calculated via gas-grain sputtering using the Draine & Salpeter prescription - a dust grain has a lifespan,  $\tau$ , which is dependent on the grain radius, as the grain loses radius proportional to its loss in mass; assuming a spherical grain, the rate of change in mass and radius can be calculated such that:

$$\tau_D = 1 \text{ Myr} \times \frac{a}{n_g}, \quad (5.2a)$$

$$\frac{da}{dt} = -\frac{a}{\tau_D}, \quad (5.2b)$$

$$\frac{dm}{dt} = -1.33 \times 10^{-13} a^2 n_g n_d \rho_{Gr}, \quad (5.2c)$$

### 5.2.3 Simulated systems

The systems being simulated in this paper are the persistent dust forming systems WR 98a and WR 104, as well as the periodic dust forming system WR 140. All of these systems were

selected as they are well documented, face-on systems with detailed observations in the Infrared. Additionally, these systems have a number of characteristics that are important for scientific purposes as well as for evaluation of the dust model.

System	Periodic	$\dot{M}_{WR}$ ( $M_{\odot} \text{ yr}^{-1}$ )	$\dot{M}_{OB}$ ( $M_{\odot} \text{ yr}^{-1}$ )	$v_{WR}^{\infty}$ ( $\text{km s}^{-1}$ )	$v_{OB}^{\infty}$ ( $\text{km s}^{-1}$ )	$\eta$ (AU)	$\chi_{\min}$
WR 98a	No	$5.0 \times 10^{-6}$	$5.0 \times 10^{-8}$	900	2000	0.0222	0.7970
WR 104	No	$3.0 \times 10^{-5}$	$6.0 \times 10^{-8}$	1220	2000	0.0033	0.2430
WR 140	Yes	$5.7 \times 10^{-5}$	$1.6 \times 10^{-6}$	2860	3200	0.0314	2.6866

**Table 5.1:** Wind properties of systems simulated in this paper.

System	Period (d)	Eccentricity ( $e$ )	$M_{WR}$ ( $M_{\odot}$ )	$M_{OB}$ ( $M_{\odot}$ )	Periastron (AU)	Apastron (AU)
WR 98a	556	0.000	10.0	18.0	4.06	4.06
WR 104	245	0.060	10.0	20.0	2.20	2.48
WR 140	2869	0.896	14.9	35.9	1.53	26.9

**Table 5.2:** Orbital properties of systems simulated in this paper.

WR 98a is a typical dusty CWB system that was primarily chosen for simulation as it is one of the only CWB systems whose dust dynamics have been simulated in an academic paper (Hendrix et al., 2016). The model utilised in Hendrix et al. was a dual-fluid model with an Epstein drag function in order to detail how dust flows through the system itself. As such, this model does not simulate dust accretion or cooling, and only deposits dust grains with a single set grain radius and a fixed dust production rate of  $\phi = 0.0763$ . However, this still provides a useful point of comparison to evaluate this papers dust model against an established model with concrete data. Furthermore, a simplified version of WR 98a was used to test the dust model and was used as a basis to explore the parameter space of dusty CWB systems by varying wind parameters and orbital separation. The parameters detailed in table 5.1 are adopted from Hendrix et al., similarly to this paper a perfectly circular orbit is assumed.

WR 104 is an archetypical dust forming binary system that is extensively observed, with multiple papers on the dynamics and formation of dust in the system.

WR 104 represents the high end of dust formation in CWB systems, with a high dust formation rate in the order of  $3 \times 10^{-7} M_{\odot} \text{ yr}^{-1}$ , the close separation of the binary system

## 5. HYDRODYNAMICAL SIMULATIONS OF WCD SYSTEMS

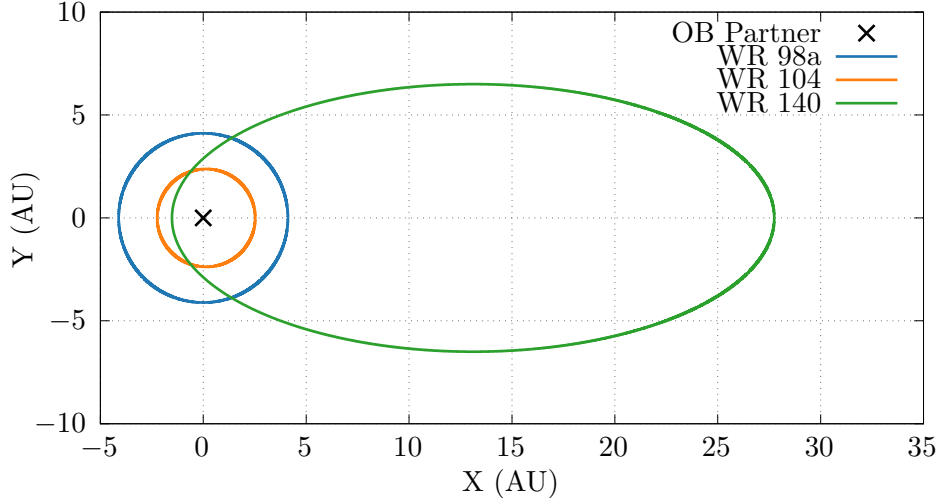


**Figure 5.1:** Orbital paths for each system, a co-ordinate transform is applied such that the orbitally dominant OB partner is always at co-ordinate (0,0). WR 140 has a significantly more eccentric orbit, as well as a much longer orbital period.

combined with the high mass loss rate results in a much lower value of  $\chi$  for the WR wind, suggesting very strong cooling in the post-shock wind collision region. As such this system is more difficult to simulate, as a higher resolution and lower Courant number are required in order to reliably simulate the post-shock cooling effect. The orbital and wind parameters of this system were derived from Soulain et al., 2018 and Harries et al., 2004.

WR 140 was simulated for this experiment as it represents an archetypical episodic CWB system, whose infrared dust emission peaks around periastron passage. WR 140 deviates from WR 98a and WR 104 by being extremely eccentric, which significantly effects the cooling parameter as the orbit progresses (figure 5.2). Additionally, the minimum value for  $\chi$  is significantly larger than the other systems, and hence cooling would be less dominant on the dynamics of the WCR, even at periapsis. Though these simulations do not calculate wind acceleration due to radiative line driving, both stellar winds are expected to be accelerated close to their terminal wind velocities (Lamers & Cassinelli, 1999). However, this discrepancy should be noted when considering the results of this paper. The orbital and wind parameters of this system were derived from work by Monnier et al., 2011, Usov, 1991, as well as Thomas et al., 2021.

Significant challenges are involved in simulating the WR 140 system compared to the other

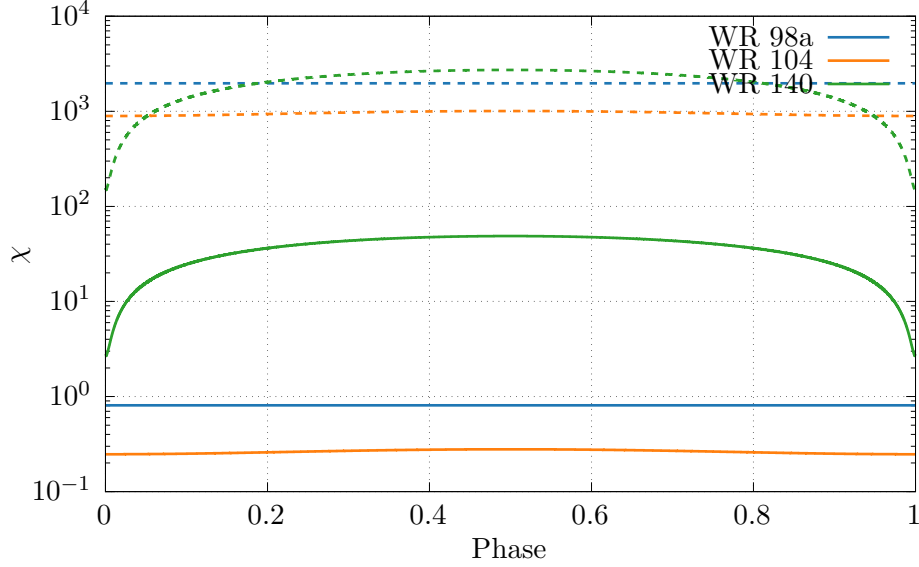


**Figure 5.2:** Change in WR cooling parameter  $\chi$  over a single orbit, solid lines represent the primary WC star, while dashed lines represent their OB partners. The dynamics of the WCR for WR 98a and WR 104 is dominated by cooling throughout their entire orbits, while WR 140 is adiabatic for most of its orbit. Additionally OB stars have significantly higher cooling parameters, and thus their flows behave adiabatically.

systems in this paper. The highly eccentric orbit of this system means that in order to simulate a full orbit of this system, a large section of the simulation would need to be rendered at full resolution, resulting much shorter timesteps and a significantly larger processor and memory requirement. This is impractical considering the time constraints of this project. In order to alleviate this issue the system was simulated with Adaptive Mesh Refinement (AMR) conditions instead of SMR. The region surrounding the stars orbit was refined and de-refined in order to ensure that there were at least 128 cells of finest size separating the stars. Additional refinement rules were established to progressively lower the grid resolution further out from the stars, as well as to ensure that the collision region was properly resolved.

#### 5.2.4 Radiative transfer modelling



## 5. HYDRODYNAMICAL SIMULATIONS OF WCD SYSTEMS

---

---

# CHAPTER 6

---

Final Notes and Conclusion

## **6. FINAL NOTES AND CONCLUSION**

---

---

# APPENDIX A

---

Astrophysical Shocks

## A. ASTROPHYSICAL SHOCKS

---

# BIBLIOGRAPHY

## Book Sources

- Carroll, B. W. & Ostlie, D. A. (2014). *An Introduction to Modern Astrophysics* (Second international). Pearson  
OCLC: 868368508.
- Dyson, J. E. (2021). *The physics of the interstellar medium* (Third edition.). CRC Press.
- Lamers, H. J. & Cassinelli, J. P. (1999). *Introduction to stellar winds*. Cambridge University Press.
- Oswalt, T. D. & Barstow, M. A. (Eds.). (2013). *Planets, Stars and Stellar Systems*. Springer Netherlands. <https://doi.org/10.1007/978-94-007-5615-1>
- Ryan, S. G. & Norton, A. J. (2010). *Stellar evolution and nucleosynthesis*. Cambridge University Press  
OCLC: ocn437083016.
- Rybicki, G. B. & Lightman, A. P. (2004). *Radiative processes in astrophysics*. Wiley  
OCLC: 255501661.
- Salaris, M. & Cassisi, S. (2005). *Evolution of Stars and Stellar Populations*.
- Spitzer Jr., L. (2008, November 20). *Physical Processes in the Interstellar Medium*. John Wiley & Sons.
- Vink, J. S. (Ed.). (2015). *Very Massive Stars in the Local Universe* (Vol. 412). Springer International Publishing. <https://doi.org/10.1007/978-3-319-09596-7>
- Ward-Thompson, D. & Whitworth, A. P. (2011). *An Introduction to Star Formation*. Cambridge University Press. <https://doi.org/10.1017/CBO9780511974021>

## BIBLIOGRAPHY

---

### Journal Sources

- Castor, J. I., Abbott, D. C. & Klein, R. I. (1975). Radiation-driven winds in Of stars. *The Astrophysical Journal*, 195, 157. <https://doi.org/10.1086/153315>
- Cherepashchuk, A. M. (1976). Detectability of Wolf-Rayet binaries from X-rays. *Soviet Astronomy Letters*, 2, 138.
- Crowther, P. A. (2003). Dust Formation around Wolf-Rayet Stars. *Astrophysics and Space Science*, 285(3), 677–685. <https://doi.org/10.1023/A:1026157126395>
- Crowther, P. A. (2007). Physical Properties of Wolf-Rayet Stars. *Annual Review of Astronomy and Astrophysics*, 45(1), 177–219. <https://doi.org/10.1146/annurev.astro.45.051806.110615>
- Draine, B. & Salpeter, E. (1979). Destruction mechanisms for interstellar dust. *The Astrophysical Journal*, 231, 438–455.
- Dwek, E. & Werner, M. W. (1981). The Infrared Emission From Supernova Condensates. *The Astrophysical Journal*, 248, 138. <https://doi.org/10.1086/159138>
- Eichler, D. & Usov, V. (1993). Particle acceleration and nonthermal radio emission in binaries of early-type stars. *The Astrophysical Journal*, 402, 271–279. <https://doi.org/10.1086/172130>
- Grimaldo, E., Reimer, A., Kissmann, R., Niederwanger, F. & Reitberger, K. (2019). Proton Acceleration in Colliding Stellar Wind Binaries. *The Astrophysical Journal*, 871, 55. <https://doi.org/10.3847/1538-4357/aaf6ee>
- Harries, T. J., Monnier, J. D., Symington, N. H. & Kurosawa, R. (2004). Three-dimensional dust radiative-transfer models: The Pinwheel Nebula of WR 104. *Monthly Notices of the Royal Astronomical Society*, 350(2), 565–574. <https://doi.org/10.1111/j.1365-2966.2004.07668.x>
- Hendrix, T., Keppens, R., van Marle, A. J., Camps, P., Baes, M. & Meliani, Z. (2016). Pinwheels in the sky, with dust: 3D modelling of the Wolf-Rayet 98a environment. *Monthly Notices of the Royal Astronomical Society*, 460(4), 3975–3991. <https://doi.org/10.1093/mnras/stw1289>
- Le Teuff, Y. H. (2002). A Model of Dust Formation in Clumpy Wolf-Rayet Winds. 260, 223.
- Lucy, L. B. & Solomon, P. M. (1970). Mass Loss by Hot Stars. *The Astrophysical Journal*, 159, 879. <https://doi.org/10.1086/150365>
- Marchenko, S. V., Moffat, A. F. J. & Crowther, P. A. (2010). Population I Wolf-Rayet Runaway Stars: The Case of WR124 and its Expanding Nebula M1-67. *The Astrophysical Journal*,

- 724, L90–L94. <https://doi.org/10.1088/2041-8205/724/1/L90>  
 ADS Bibcode: 2010ApJ...724L..90M
- Monnier, J. D., Zhao, M., Pedretti, E., Millan-Gabet, R., Berger, J.-P., Traub, W., Schloerb, F. P., ten Brummelaar, T., McAlister, H., Ridgway, S., Sturmman, L., Sturmman, J., Turner, N., Baron, F., Kraus, S., Tannirkulam, A. & Williams, P. M. (2011). First Visual Orbit for the Prototypical Colliding-wind Binary WR 140. *The Astrophysical Journal Letters*, 742, L1. <https://doi.org/10.1088/2041-8205/742/1/L1>
- Neugent, K. & Massey, P. (2019). The Wolf–Rayet Content of the Galaxies of the Local Group and Beyond. *Galaxies*, 7(3), 74. <https://doi.org/10.3390/galaxies7030074>
- Prilutskii, O. F. & Usov, V. V. (1976). X rays from Wolf-Rayet binaries. *Soviet Astronomy*, 20, 2.
- Rosslowe, C. K. & Crowther, P. A. (2015). Spatial distribution of Galactic Wolf–Rayet stars and implications for the global population. *Monthly Notices of the Royal Astronomical Society*, 447(3), 2322–2347. <https://doi.org/10.1093/mnras/stu2525>
- Schure, K. M., Kosenko, D., Kaastra, J. S., Keppens, R. & Vink, J. (2009). A New Radiative Cooling Curve Based on an Up-To-Date Plasma Emission Code. *Astronomy & Astrophysics*, 508(2), 751–757. <https://doi.org/10.1051/0004-6361/200912495>
- Soulain, A., Millour, F., Lopez, B., Matter, A., Lagadec, E., Carbillet, M., Camera, A., Lamberts, A., Langlois, M., Milli, J., Avenhaus, H., Magnard, Y., Roux, A., Moulin, T., Carle, M., Sevin, A., Martinez, P., Abe, L. & Ramos, J. (2018, June 22). *The SPHERE view of Wolf-Rayet 104*. arXiv: 1806.08525 [astro-ph]. Retrieved October 23, 2018, from <http://arxiv.org/abs/1806.08525>
- Spiteri, R. J. & Ruuth, S. J. (2002). A New Class of Optimal High-Order Strong-Stability-Preserving Time Discretization Methods. *SIAM Journal on Numerical Analysis*, 40(2), 469–491. <https://doi.org/10.1137/S0036142901389025>
- Stevens, I. R., Blondin, J. M. & Pollock, A. M. T. (1992). Colliding winds from early-type stars in binary systems. *The Astrophysical Journal*, 386, 265–287. <https://doi.org/10.1086/171013>
- Stone, J. M., Tomida, K., White, C. J. & Felker, K. G. (2020). The Athena++ Adaptive Mesh Refinement Framework: Design and Magnetohydrodynamic Solvers. *The Astrophysical Journal Supplement Series*, 249(1), 4. <https://doi.org/10.3847/1538-4365/ab929b>
- Thomas, J. D., Richardson, N. D., Eldridge, J. J., Schaefer, G. H., Monnier, J. D., Sana, H., Moffat, A. F. J., Williams, P., Corcoran, M. F., Stevens, I. R., Weigelt, G., Zainol,



## BIBLIOGRAPHY

---

- F. D., Anugu, N., Le Bouquin, J.-B., ten Brummelaar, T., Campos, F., Couperus, A., Davies, C. L., Ennis, J., ... Zurmühl, U. (2021). The orbit and stellar masses of the archetype colliding-wind binary WR 140. *Monthly Notices of the Royal Astronomical Society*, 504(4), 5221–5230. <https://doi.org/10.1093/mnras/stab1181>
- Usov, V. V. (1991). Stellar wind collision and dust formation in long-period, heavily interacting Wolf-Rayet binaries. *Monthly Notices of the Royal Astronomical Society*, 252(1), 49–52. <https://doi.org/10.1093/mnras/252.1.49>
- Williams, P. M. (2008). Dust formation by colliding-wind binaries. 33, 71–76.
- Williams, P. M. & van der Hucht, K. A. (2015). The colliding-wind WC9+OB system WR 65 and dust formation by WR stars, 275–278.